

## RESEARCH ARTICLE SUMMARY

## MICROBIOLOGY

# PIM1 controls GBP1 activity to limit self-damage and to guard against pathogen infection

Daniel Fisch, Moritz M. Pfeleiderer, Eleni Anastasakou, Gillian M. Mackie, Fabian Wendt, Xiangyang Liu, Barbara Clough, Samuel Lara-Reyna, Vesela Encheva, Ambrosius P. Snijders, Hironori Bando, Masahiro Yamamoto, Andrew D. Beggs, Jason Mercer, Avinash R. Shenoy, Bernd Wollscheid, Kendle M. Maslowski, Wojtek P. Galej, Eva-Maria Frickel\*

**INTRODUCTION:** Cells in infected tissues are exposed to inflammatory stimuli, including the innate and adaptive immunity-stimulating cytokine interferon- $\gamma$  (IFN- $\gamma$ ). Although most tissue-resident and infiltrating cells are not infected, when exposed to IFN- $\gamma$ , these bystander cells preemptively express a repertoire of interferon-stimulated genes (ISGs) with robust antimicrobial activities and the potential for self-harm. ISGs of the guanylate-binding protein (GBP) family are large, membrane-active guanosine triphosphatases (GTPases). GBPs can control intracellular microbes in various ways, most importantly by promoting membrane rupture and the release of microbial ligands and by the induction of programmed cell death, including pyroptosis and apoptosis. How uninfected cells protect themselves from the potentially self-destructive actions of GBPs while keeping these proteins readily available to combat infection is unknown.

**RATIONALE:** Cells need to tightly control the activity of antimicrobial proteins but rapidly deploy them upon infection. How is this achieved in human cells? Posttranslational modifications, such as phosphorylation by protein kinases, enable rapid and precise control of protein activities. We studied the phosphorylation of GBP1, a typical ISG, and how this modification affects its function, activity, and localization in human macrophages.

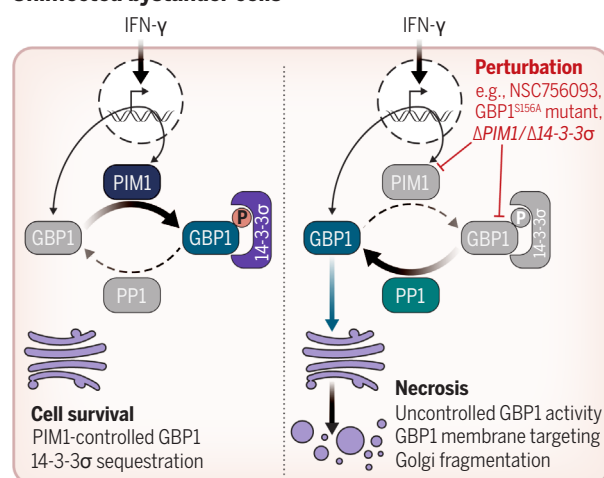
**RESULTS:** Ectopic expression of GBP1 in human macrophages led to changes in cell morphology, GBP1 accumulation at the Golgi apparatus, Golgi fragmentation, and uncontrolled cellular necrosis. These findings illustrate GBP1's potential to inflict self-damage. This phenotype was mitigated by IFN- $\gamma$  treatment, suggesting that another IFN- $\gamma$ -inducible factor limited GBP1 activity. We identified the kinase PIM1 as being this factor. We generated a phosphorylation-specific antibody and used high-resolution

mass spectrometry to demonstrate GBP1 phosphorylation at serine-156 (Ser<sup>156</sup>), which was guided by a basophilic PIM1 recognition motif. Ser<sup>156</sup> is the central residue of a 14-3-3 protein binding motif, which suggests a switch-like function for its phosphorylation. Indeed, 14-3-3 proteins, especially 14-3-3 $\sigma$ , interacted with phosphorylated GBP1. In vitro reconstitution of this complex followed by single-particle cryo-electron microscopy confirmed a 14-3-3 $\sigma$  dimer grabbing onto the GBP1 GTPase domain. This binding locked GBP1 in a GTPase-inactive, monomeric state and restrained its activity in the macrophage cytosol. Expressing phosphorylation-deficient GBP1 mutants or mutants that could not be recognized by the kinase PIM1 or bound by 14-3-3 $\sigma$  led to uncontrolled GBP1 activation and subsequent cell death. Genetic depletion of either PIM1 or 14-3-3 $\sigma$  had similar outcomes, as did treatment with the GBP1:PIM1 interaction inhibitor NSC756093. Using the inhibitor in IFN- $\gamma$ -activated patient-derived tumor organoids increased organoid death and prevented organoid reformation. Thus, we found that PIM1 and 14-3-3 $\sigma$  together controlled the activity of GBP1 in human cells. Disrupting PIM1-driven control of GBP1 has potential therapeutic implications for cancer therapy and innate immunity.

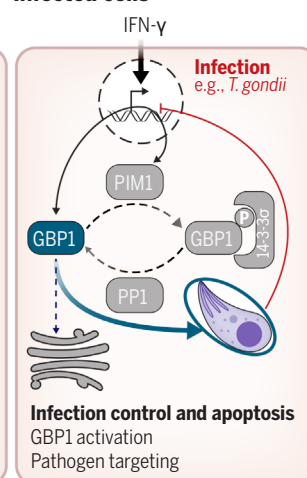
We observed that PIM1 mRNA and protein were extremely short-lived. Infection with the apicomplexan parasite *Toxoplasma gondii*, a pathogen that resides within intracellular vacuoles and blocks IFN- $\gamma$  signaling by means of the effector protein TgIST, led to fast depletion of PIM1. This in turn reduced GBP1 Ser<sup>156</sup> phosphorylation levels and liberated GBP1 from 14-3-3 $\sigma$  sequestration. High-throughput imaging revealed that GBP1 then rapidly targeted *Toxoplasma*-containing vacuoles to improve control of the infection.

**CONCLUSION:** The IFN- $\gamma$ -induced, short-lived kinase PIM1 guards the integrity of IFN- $\gamma$  signaling and protects self-membranes by regulating the activity of the potent antimicrobial effector GBP1. Pathogens that block IFN- $\gamma$  signaling, thereby reducing the levels of PIM1, are then exposed to GBP1-driven innate immune control. The phosphoregulation of GBP1 by PIM1 reveals an IFN- $\gamma$ -dependent control mechanism that protects uninfected bystander cells from self-inflicted innate immune damage during the process of pathogen elimination. ■

## Uninfected bystander cells



## Infected cells



**The protein kinase PIM1 controls GBP1 activity.** In uninfected bystander cells, IFN- $\gamma$  signaling induces expression of PIM1, which phosphorylates GBP1, subjecting it to sequestration by 14-3-3 $\sigma$ . This shunts aberrant GBP1 activity and ensures cell survival (left). Perturbation of this homeostasis leads to GBP1 dephosphorylation and Golgi targeting and disruption, culminating in necrosis (middle). Intracellular microbes that disrupt IFN- $\gamma$  signaling, e.g., *T. gondii*, deplete PIM1 and liberate GBP1, which then attacks and controls the infection (right).

The list of author affiliations is available in the full article online.  
\*Corresponding author. Email: e.frickel@bham.ac.uk  
Cite this article as D. Fisch et al., *Science* **382**, eadg2253 (2023). DOI: 10.1126/science.adg2253

**READ THE FULL ARTICLE AT**  
<https://doi.org/10.1126/science.adg2253>

## RESEARCH ARTICLE

## MICROBIOLOGY

# PIM1 controls GBP1 activity to limit self-damage and to guard against pathogen infection

Daniel Fisch<sup>1,2</sup>, Moritz M. Pfeleiderer<sup>3</sup>, Eleni Anastasakou<sup>3</sup>, Gillian M. Mackie<sup>4</sup>, Fabian Wendt<sup>5,6</sup>, Xiangyang Liu<sup>3</sup>, Barbara Clough<sup>2</sup>, Samuel Lara-Reyna<sup>2</sup>, Vesela Encheva<sup>7</sup>, Ambrosius P. Snijders<sup>7,8</sup>, Hironori Bando<sup>9,10</sup>, Masahiro Yamamoto<sup>9,10</sup>, Andrew D. Beggs<sup>11</sup>, Jason Mercer<sup>2</sup>, Avinash R. Shenoy<sup>12,13</sup>, Bernd Wollscheid<sup>5,6</sup>, Kendle M. Maslowski<sup>4,14,15,16</sup>, Wojtek P. Galej<sup>3</sup>, Eva-Maria Frickel<sup>1,2,\*</sup>

Disruption of cellular activities by pathogen virulence factors can trigger innate immune responses. Interferon- $\gamma$  (IFN- $\gamma$ )-inducible antimicrobial factors, such as the guanylate binding proteins (GBPs), promote cell-intrinsic defense by attacking intracellular pathogens and by inducing programmed cell death. Working in human macrophages, we discovered that GBP1 expression in the absence of IFN- $\gamma$  killed the cells and induced Golgi fragmentation. IFN- $\gamma$  exposure improved macrophage survival through the activity of the kinase PIM1. PIM1 phosphorylated GBP1, leading to its sequestration by 14-3-3 $\sigma$ , which thereby prevented GBP1 membrane association. During *Toxoplasma gondii* infection, the virulence protein TgIST interfered with IFN- $\gamma$  signaling and depleted PIM1, thereby increasing GBP1 activity. Although infected cells can restrain pathogens in a GBP1-dependent manner, this mechanism can protect uninfected bystander cells. Thus, PIM1 can provide a bait for pathogen virulence factors, guarding the integrity of IFN- $\gamma$  signaling.

Interferon- $\gamma$  (IFN- $\gamma$ ) is a pivotal cytokine that promotes innate and adaptive immunity during infection. IFN- $\gamma$  acts on all nucleated cells to induce expression of a large repertoire of interferon-stimulated genes (ISGs) with potent antimicrobial activities (1). Pathogens are targeted by antimicrobial pathways after their detection by pattern recognition receptors (PRRs) (pattern-triggered immunity) or when they disrupt a regulator of an immune response (effector-triggered immunity). The latter mechanism, also referred to as guard immunity, was originally described in plants and suggests that innate immunity can indi-

rectly detect virulence factors by their activities (2). The complexity of guard immunity in mammalian systems remains largely unexplored [reviewed in (3)]. Whether guard immunity exists in the context of inflammatory type II interferon production and signaling is unknown.

Among the ISGs are large guanosine triphosphatases (GTPases) of the GBP family (4). GBPs restrict infection by targeting intracellular microbes, thereby promoting their rupture and the release of microbial ligands; by redirecting autophagy and oxidative machinery to pathogen-containing compartments; and by removing replicative niches through induction of pyroptosis or apoptosis (5–15). IFN- $\gamma$  up-regulates antimicrobial genes, including GBPs, in the primary infected cells and in neighboring, uninfected bystander cells. IFN- $\gamma$  thus induces ubiquitous expression of GBPs in most cell types. Among GBPs, GBP1 is the most abundant in IFN- $\gamma$ -primed cells. GBP1 has a C-terminal prenylation site that enables its membrane association (16) and forms homo- and heterodimers and membrane-bound coatomers with itself or with other GBPs (17, 18). The GBP1 GTPase converts guanosine triphosphate (GTP) to guanosine monophosphate (GMP) in two steps (19). GBP1 can target membranes of the host Golgi apparatus (16, 20) as well as plasma membrane-derived vacuoles containing *Toxoplasma gondii* (Tg) (10, 11) or lipopolysaccharide (LPS) on cytosolic bacteria (7, 11, 13–15). However, how uninfected cells protect themselves from the potentially destructive actions of GBP1 remains unclear.

## IFN- $\gamma$ and phosphorylation control GBP1 activity and prevent cytotoxicity

To investigate how the activities of GBP1 are regulated in uninfected cells, we used a doxycycline (Dox)-inducible expression system in phorbol myristate acetate (PMA)-differentiated THP-1 macrophages (THP-1 $\Delta$ GBP1+GBP1) (11). We first measured the survival of cells that ectopically expressed GBP1 in the absence of exposure to IFN- $\gamma$ . Dox-induced ectopic expression of GBP1 was cytotoxic, progressively leading to ~75% cell loss over 7 days (Fig. 1A). Exposure of GBP1-expressing cells to IFN- $\gamma$  reduced cell loss by ~55% (Fig. 1A). Treatment with IFN- $\gamma$  in the absence of ectopic GBP1 expression resulted in minimal cell loss (Fig. 1A). Thus, we surmised that an unknown IFN- $\gamma$ -dependent process and/or protein(s) must block GBP1-driven toxicity.

GBP1 contains three putative, surface-exposed phosphorylation sites: Ser<sup>156</sup>, Ser<sup>157</sup>, and Tyr<sup>427</sup> (Fig. 1B). Immunoprecipitated Flag-GBP1 from macrophages probed for phosphorylated serine residues confirmed the presence of a phosphorylated GBP1 species, the amount of which increased upon exposure to IFN- $\gamma$  (Fig. 1C). We hypothesized that IFN- $\gamma$ -mediated phosphorylation of GBP1 could be a regulatory switch that suppresses the toxicity of GBP1. To test this possibility, we studied phosphorylation-deficient mutants of GBP1 [S156A (Ser<sup>156</sup>→Ala), S157A (Ser<sup>157</sup>→Ala), Y427F (Tyr<sup>427</sup>→Phe)] expressed in  $\Delta$ GBP1 cells (fig. S1). Whereas S157A and Y427F had no effect on the dispersed, granular appearance of GBP1 within the cytosol, GBP1<sup>S156A</sup> accumulated in perinuclear areas (fig. S2A), which were revealed to be the Golgi apparatus by immunofluorescence assays (fig. S2B). Furthermore, GBP1<sup>S156A</sup>-expressing cells were more elongated than cells expressing wild-type (WT) GBP1 (fig. S2C) and displayed changes in their cortical actin cytoskeleton (fig. S2D). Phosphorylation of GBP1 Ser<sup>156</sup> might thus control localization and activities of GBP1.

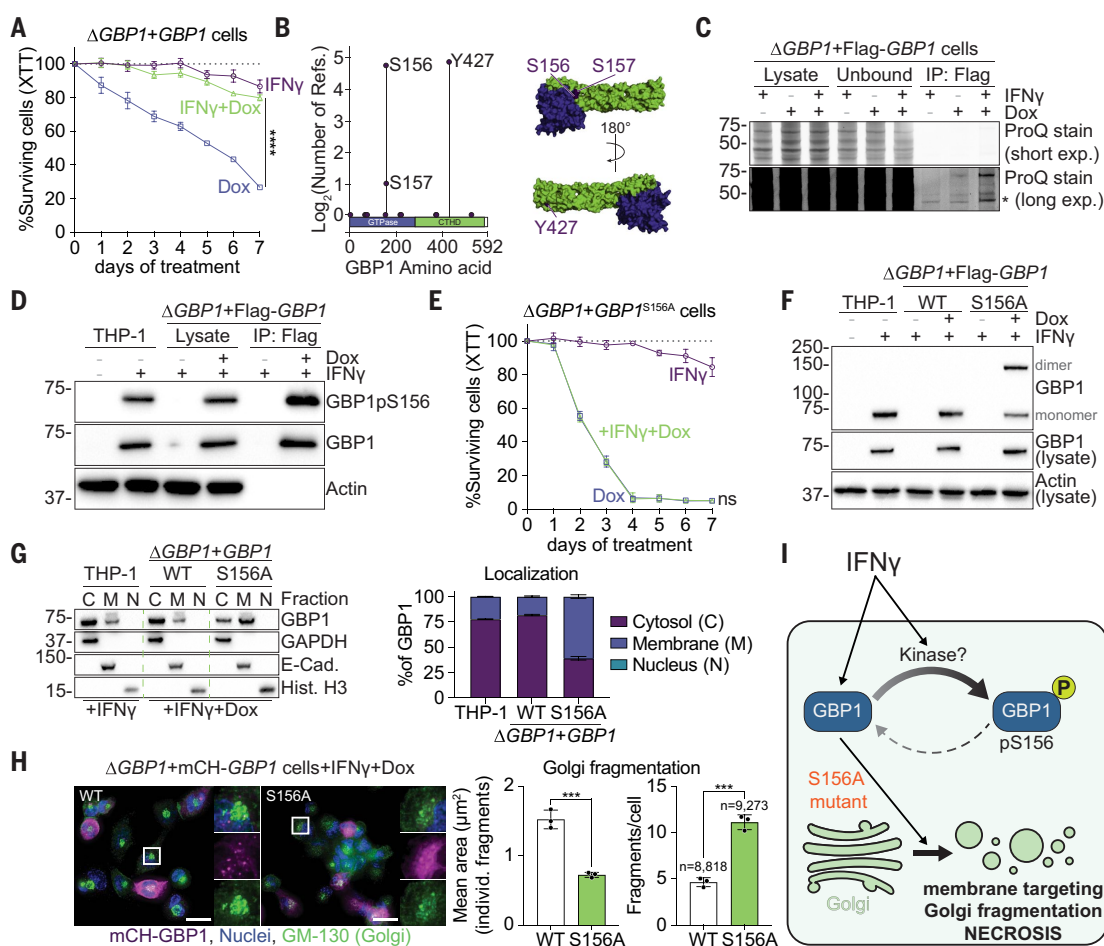
To test whether GBP1 was phosphorylated at Ser<sup>156</sup> specifically, we raised a phosphospecific antibody and validated its specificity with the following results: First, the antibody specifically interacted with phosphorylated GBP1 peptide (epitope: amino acids Ile<sup>152</sup> to Cys<sup>166</sup>); second, it bound to immunoprecipitated Flag-GBP1 WT but not Flag-GBP1<sup>S156A</sup>; third, with the exception of minor reactivity toward GBP3, the antibody showed no cross-reactivity with other GBPs; and fourth, it specifically stained mCherry-tagged GBP1 (mCH-GBP1) but not mCH-GBP1<sup>S156A</sup> in immunofluorescence assays (fig. S3, A to D). Using this antibody, we confirmed that GBP1 was phosphorylated at Ser<sup>156</sup> upon exposure of cells to IFN- $\gamma$  by immunoprecipitation and immunoblot assays (Fig. 1D). Expression of GBP1<sup>S156A</sup> was more toxic than that of WT GBP1, and IFN- $\gamma$  treatment no longer suppressed the toxicity of GBP1<sup>S156A</sup> (Fig. 1E). We thus checked

<sup>1</sup>Host-*Toxoplasma* Interaction Laboratory, The Francis Crick Institute, London, UK. <sup>2</sup>Institute of Microbiology and Infection, School of Biosciences, University of Birmingham, Edgbaston, UK. <sup>3</sup>European Molecular Biology Laboratory, 71 Avenue des Martyrs, Grenoble, France. <sup>4</sup>Institute of Immunology and Immunotherapy, University of Birmingham, Edgbaston, UK. <sup>5</sup>Department of Health Sciences and Technology (D-HEST), ETH Zürich, Institute of Translational Medicine (ITM), Zürich, Switzerland. <sup>6</sup>Swiss Institute of Bioinformatics (SIB), Lausanne, Switzerland. <sup>7</sup>Mass Spectrometry and Proteomics Platform, The Francis Crick Institute, London, UK. <sup>8</sup>Bruker Nederland BV, Leiderdorp, Netherlands. <sup>9</sup>Department of Immunoparasitology, Research Institute for Microbial Diseases, Osaka University, Osaka, Japan. <sup>10</sup>Laboratory of Immunoparasitology, WPI Immunology Frontier Research Center, Osaka University, Osaka, Japan. <sup>11</sup>Institute of Cancer and Genomic Sciences, University of Birmingham, Edgbaston, UK. <sup>12</sup>MRC Centre for Molecular Bacteriology and Infection, Department of Infectious Disease, Imperial College London, London, UK. <sup>13</sup>Inflammasome Biology Laboratory, The Francis Crick Institute, London, UK. <sup>14</sup>Institute of Metabolism and Systems Research, University of Birmingham, Edgbaston, UK. <sup>15</sup>Cancer Research UK Beatson Institute, Glasgow, UK. <sup>16</sup>School of Cancer Sciences, University of Glasgow, Glasgow, UK.

\*Corresponding author. Email: e.frickel@bham.ac.uk

**Fig. 1. IFN- $\gamma$  and phosphorylation control GBP1 cytotoxicity and activity.**

(A) XTT cell survival assay of THP-1 $\Delta$ GBP1+GBP1 WT cells treated with IFN- $\gamma$  with or without Dox for the indicated number of days. (B) Graph (left) and GBP1 structure (right) showing predicted phosphorylation sites and their surface-localization based on data from proteomics references (Refs). CTHD, C-terminal helical domain. (C) Images with short or long exposure (exp.) for a ProQ-Diamond phosphoprotein stain for immunoprecipitated Flag-GBP1 from THP-1 $\Delta$ GBP1+Flag-GBP1 cells treated with IFN- $\gamma$  with or without Dox. The asterisk indicates background bands. IP, immunoprecipitation. (D) Immunoblots using GBP1pS156 antibody showing phosphorylation of GBP1 in IFN- $\gamma$ - and Dox-treated THP-1 $\Delta$ GBP1+Flag-GBP1. (E) XTT cell survival assay of THP-1 $\Delta$ GBP1+GBP1<sup>S156A</sup> cells treated with IFN- $\gamma$  with or without Dox for the indicated number of days. (F) Immunoblot analysis of GBP1 oligomerization in cross-linked pellets and in cell lysates. (G) Immunoblots of subcellular fractionation to determine GBP1 localization in IFN- $\gamma$ -primed THP-1 WT or  $\Delta$ GBP1+GBP1 cells expressing GBP1<sup>S156A</sup> or WT GBP1 with markers for the cytosol (C), membranes (M), or the nucleus (N) (left) and quantification (right). E-Cad., E-cadherin; GAPDH, glyceraldehyde phosphate dehydrogenase. (H) Immunofluorescence images of cells expressing mCH-GBP1 WT or mCH-GBP1<sup>S156A</sup> for 48 hours and stained for Golgi marker GM130 (left) and quantification of mean area and number of Golgi fragments (right). The number of quantified cells is indicated in the figure. The



smaller images on the right are zoomed-in views of the regions outlined by the white rectangles. Scale bars are 20  $\mu$ m. Green, GM-130 (Golgi); magenta, mCH-GBP1; blue, nuclei. (I) Graphic summarizing findings on GBP1 activity control. Data information: Images in (C) and (D) and (F) to (H) are representative of  $n = 3$  experiments. Graphs in (A), (E), (G), and (H) show mean  $\pm$  SEM from  $n = 3$  experiments. \*\*\* $P \leq 0.001$  and \*\*\*\* $P < 0.0001$  for the indicated comparisons in (A) and (E) from one-way analysis of variance (ANOVA) and in (H) from unpaired Student's  $t$  tests; ns is not significant. For gel source data, see data S5.

macrophages that expressed WT GBP1 or GBP1<sup>S156A</sup> for markers of regulated cell death (fig. S4A) but did not observe any hallmarks of apoptosis, necroptosis, or pyroptosis after 2, 4, or 7 days (fig. S4B). Chemical inhibition of regulated cell-death pathways failed to prevent cells from dying over 4 days of constitutive ectopic expression of GBP1 (fig. S4C). Again, addition of IFN- $\gamma$  rescued cells that expressed WT GBP1 but not GBP1<sup>S156A</sup> and minimally affected cell viability by itself (fig. S4C). Thus, GBP1 phosphorylation on Ser<sup>156</sup> was required to prevent unwanted toxicity and unregulated, necrotic death of human macrophages.

We next asked whether phosphorylation of GBP1 on Ser<sup>156</sup> affects its known activities, such as oligomerization (14, 17, 18) and membrane association (16). Immunoblots showed that

cytosolic WT GBP1 was monomeric, whereas GBP1<sup>S156A</sup> dimers were readily detected, which is suggestive of increased GBP1 activity (Fig. 1F). Subcellular fractionation showed increased membrane association of GBP1<sup>S156A</sup> (Fig. 1G). Because GBP1<sup>S156A</sup> also exhibited increased Golgi targeting (fig. S2B), we next assessed Golgi morphology after 2 days of continuous GBP1 expression. We observed increased fragmentation of the Golgi in cells that expressed GBP1<sup>S156A</sup> as compared with cells that expressed WT GBP1; the cells that expressed GBP1<sup>S156A</sup> showed  $\sim 2.5$  times more fragments per cell with a decreased average fragment size (Fig. 1H). Taken together, the phosphodeficient GBP1<sup>S156A</sup> mutant showed increased association with and disruption of the Golgi, which was accompanied by unregulated cellular necrosis. Thus, Ser<sup>156</sup> phosphorylation suppresses

GBP1 activities and protects cells from self-inflicted damage (Fig. 1I).

### The kinase PIM1 phosphorylates GBP1 at Ser<sup>156</sup>

To narrow down the number of kinases that are capable of phosphorylating GBP1 on Ser<sup>156</sup>, we first used in silico analysis, which identified nine candidate protein kinases (fig. S5A). For each of these kinases, we confirmed expression in macrophages by reverse transcription quantitative polymerase chain reaction (RT-qPCR) and reduced their expression with small interfering RNA (siRNA) silencing (figs. S5B and S6). Next, we immunoprecipitated Flag-GBP1 from THP-1 cells transfected with siRNAs directed against the kinases or against protein phosphatase 1/2 catalytic subunit alpha (PPP1CA, PPP2CA; Fig. 2A). Quantification of phosphoproteins suggested a reduction in



**Fig. 2. The kinase PIM1 phosphorylates GBP1 at Ser<sup>156</sup>.**

**(A)** Immunoblots and silver or ProQ-Diamond phosphoprotein stain of immunoprecipitated Flag-GBP1 WT from IFN- $\gamma$ - and Dox-treated THP-1 $\Delta$ GBP1+Flag-GBP1 cells transfected with siRNA for the indicated genes. Quantification shows the change in total GBP1 phosphorylation (top) and the change in GBP1 Ser<sup>156</sup> phosphorylation (bottom) normalized to siRNA control (siCTRL)-transfected cells.

**(B)** Immunoblot and silver stain of *in vitro* kinase assays with PIM family kinases with or without 10  $\mu$ M ATP. The asterisk indicates unspecific protein bands. **(C)** Immunoblots after cross-linking and immunoprecipitation of Flag-GBP1 from THP-1 $\Delta$ GBP1+Flag-GBP1 cells treated with IFN- $\gamma$  with or without Dox and GBP1:PIM1 interaction inhibitor NSC756093.

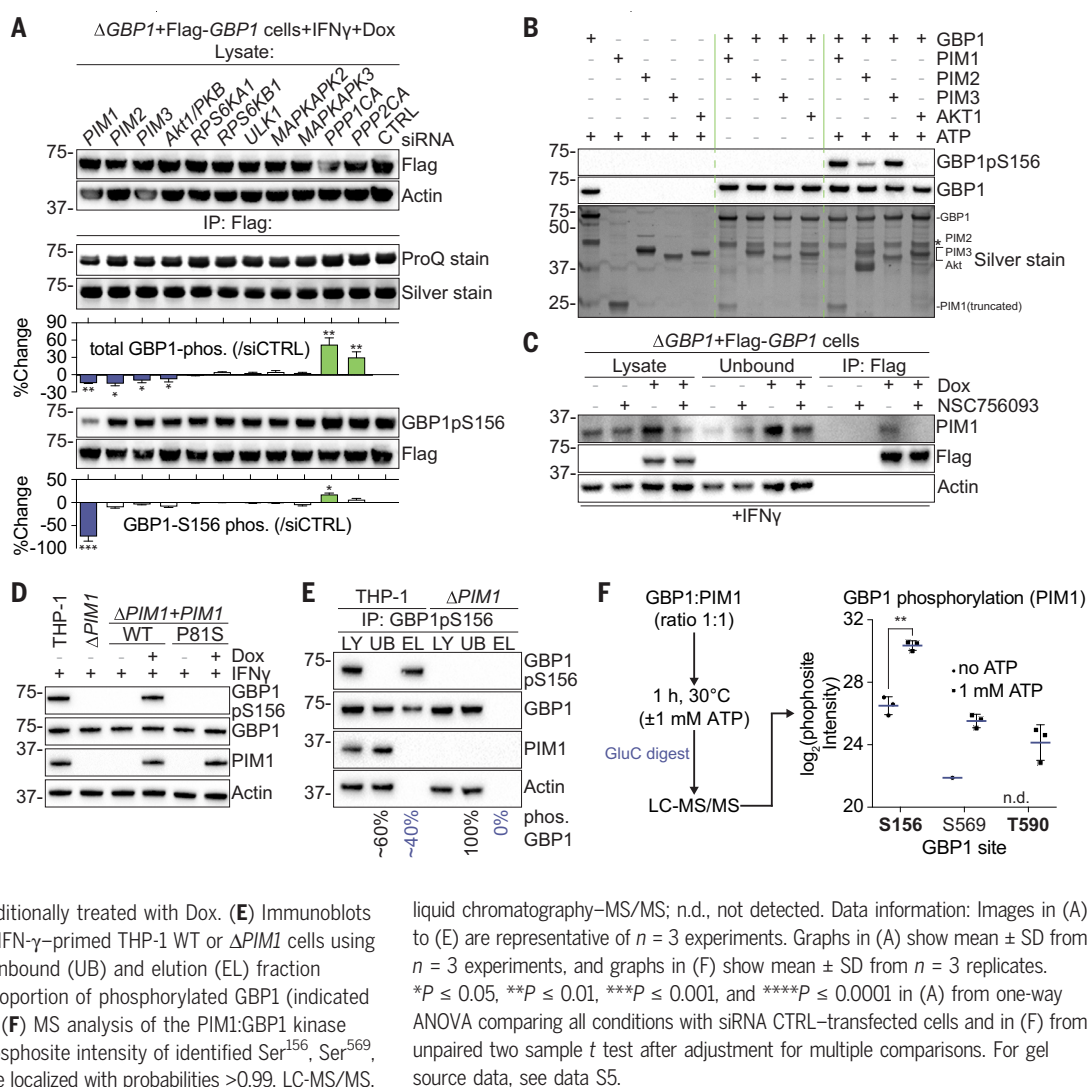
**(D)** Immunoblots testing for phosphorylation of endogenous GBP1 in IFN- $\gamma$ -primed THP-1 WT or  $\Delta$ PIM1 macrophages reconstituted with PIM1 WT or a

kinase-dead mutant (P81S) and additionally treated with Dox. **(E)** Immunoblots of GBP1 immunoprecipitation from IFN- $\gamma$ -primed THP-1 WT or  $\Delta$ PIM1 cells using GBP1pS156 antibody. Volumes of unbound (UB) and elution (EL) fraction were equalized to determine the proportion of phosphorylated GBP1 (indicated below the immunoblot). LY, lysate. **(F)** MS analysis of the PIM1:GBP1 kinase assay. The plot depicts the  $\log_2$  phosphosite intensity of identified Ser<sup>156</sup>, Ser<sup>569</sup>, and Thr<sup>590</sup> sites of GBP1, which were localized with probabilities >0.99. LC-MS/MS.

total phosphorylation of GBP1 when PIM-family kinases were silenced, whereas silencing of *PPP1CA* or *PPP2CA* increased its total phosphorylation levels (Fig. 2A). Immunoblots using the Ser<sup>156</sup> phosphospecific antibody showed that loss of PIM1 most strongly reduced phosphorylation of GBP1 at this residue (Fig. 2A). We next tested whether PIM family kinases could directly phosphorylate GBP1. Indeed, recombinant PIM1, 2, or 3 all phosphorylated GBP1 to varying degrees in vitro (Fig. 2B). Furthermore, we confirmed a previously observed direct interaction between PIM1 and GBP1 (21) in IFN- $\gamma$ -exposed THP-1 cells after cross-linking and immunoprecipitation. The PIM1:GBP1 interaction inhibitor NSC756093 abolished this interaction (Fig. 2C). Next, we generated THP-1 $\Delta$ PIM1 CRISPR-Cas9 knockout cells and confirmed the knockout of PIM1 by immunoblotting and RT-qPCR (fig. S7A). Endogenous GBP1 was not phosphorylated at Ser<sup>156</sup> in IFN- $\gamma$ -exposed  $\Delta$ PIM1 cells, and phosphorylation was restored upon reconstitution with PIM1 WT but not

with a PIM1 kinase-dead mutant [PIM1<sup>P81S</sup> (22); Fig. 2D and fig. S7B]. Immunoprecipitation of endogenous GBP1 from IFN- $\gamma$ -exposed THP-1 WT cells with the phosphospecific antibody showed that ~40% of the cellular GBP1 pool was phosphorylated (Fig. 2E).

PIM1, 2, and 3 are >65% similar to each other but vary in their efficiency of GBP1 phosphorylation (Fig. 2, A and B). To assess whether PIM2 and 3 also play a role in cellulose, we compared their expression levels in naïve and IFN- $\gamma$ -treated macrophages by RT-qPCR and immunoblotting. Only PIM1 showed IFN- $\gamma$  inducibility (fig. S8A), confirming previous findings (23). Knockout of PIM1 did not influence the kinetics or magnitude of GBP1 expression (fig. S8B), but endogenous GBP1 was no longer phosphorylated at Ser<sup>156</sup> in  $\Delta$ PIM1 cells (Fig. 2D and fig. S8C). Additional depletion of PIM2 or PIM3 in  $\Delta$ PIM1 cells had no influence on phosphorylation of GBP1 as determined by immunoblotting (fig. S8C). However, immunoprecipitation and ProQ stain of endoge-



liquid chromatography–MS/MS; n.d., not detected. Data information: Images in (A) to (E) are representative of  $n = 3$  experiments. Graphs in (A) show mean  $\pm$  SD from  $n = 3$  experiments, and graphs in (F) show mean  $\pm$  SD from  $n = 3$  replicates. \* $P \leq 0.05$ , \*\* $P \leq 0.01$ , \*\*\* $P \leq 0.001$ , and \*\*\*\* $P \leq 0.0001$  in (A) from one-way ANOVA comparing all conditions with siRNA CTRL–transfected cells and in (F) from unpaired two sample  $t$  test after adjustment for multiple comparisons. For gel source data, see data S5.

nous GBP1 from  $\Delta PIM1$  cells showed that the protein remained phosphorylated at residues other than Ser<sup>156</sup> (fig. S8D).

Because PIM1 showed a prominent effect on the phosphorylation of GBP1 and is a known GBP1 interactor in cancer cells, we performed additional experiments with recombinant PIM1 and GBP1 to explore their interaction. These experiments showed a concentration-dependent increase in the phosphorylation of GBP1 by PIM1, which was abolished by inclusion of NSC756093, corroborating a requirement for direct interaction between the two proteins (fig. S8E). High-resolution mass spectrometry (MS) enabled dissection of the PIM1 kinase–GBP1 substrate relationship and identified three phosphorylation sites (Ser<sup>156</sup>, Ser<sup>569</sup>, and Thr<sup>590</sup>; Fig. 2F). Fragment peak annotation of the electron-transfer dissociation (ETD)-activated tandem MS (MS/MS) spectra for the corresponding monophosphorylated peptides unequivocally confirmed phosphorylation at Ser<sup>156</sup> and Thr<sup>590</sup> (MaxQuant PTM site

localization probability >0.9999; fig. S8F and data S1). Ser<sup>156</sup> phosphorylation increased by 14-fold upon the addition of adenosine triphosphate (ATP), firmly establishing PIM1 as a bona fide GBP1 kinase.

We next sought to identify the PIM1 recognition sequence within GBP1. Evolutionary analysis of >3300 eukaryotic *GBP* genes identified the closest GBP1 homologs in 484 species (fig. S9A and data S2). Most of the analyzed organisms also had a well-conserved PIM1 homolog (data S2). The GBP1 homologs were analyzed for the presence of the corresponding phosphoserine, and the amino acid sequence upstream of the putative phosphoserine residue was compared with previously reported PIM1 recognition motifs (24–27). From this, it appeared that a basophilic kinase substrate motif (R<sup>151</sup>XRKS<sup>156</sup>, where R is Arg, X is any residue, K is Lys, and S is Ser) was required for recognition of GBP1 by PIM1 (fig. S9A). The PIM1 motif and the putative phosphorylation site (residue equivalent to Ser<sup>156</sup>) were well conserved across evolution, and their appearance in GBP sequences correlated with each other (fig. S9A). We used a series of GBP1 mutants (fig. S1) to assess the functional role of this motif in guiding Ser<sup>156</sup> phosphorylation. We observed a complete loss of Ser<sup>156</sup> phosphorylation in K155A or R153A mutants and reduced phosphorylation for R151A (fig. S9B). Because Lys<sup>155</sup> and Arg<sup>153</sup> lie within the phosphospecific antibody epitope, their mutation could impair antibody binding. We thus used phosphoprotein-specific staining to assess phosphorylation independently. GBP1<sup>K155A</sup> had residual phosphoprotein-specific staining levels similar to that of GBP1<sup>S156A</sup>, whereas GBP1<sup>R153A</sup> or GBP1<sup>R151A</sup> showed only a ~40% reduction (fig. S9B). Similarly, GBP1<sup>R151A/R153A</sup> and all mutants including K155A displayed reduced levels of phosphorylation, which were similar to the residual level of S156A (fig. S9B). Thus, the PIM1 phosphorylation motif in GBP1 is a basophilic kinase substrate motif.

Having established the GBP1 recognition motif for PIM1, we next assessed the other human GBP family members (fig. S9C). From this, it appeared that only GBP3, which is expressed at low levels in human macrophages (11), possesses a functional motif. All other GBPs have disruptive amino acid replacements in the recognition motif (GBP2, 4, 6, and 7) or a mutated phosphorylation acceptor site (GBP5; fig. S9C). We next tested the importance of PIM1 on cellular survival. In  $\Delta$ PIM1 cells, IFN- $\gamma$  stimulation alone was sufficient to induce gradual cell loss over 7 days (fig. S9D), which resembled ectopic expression of WT GBP1 in naïve cells (Fig. 1A). Notably, the silencing of GBP1, but no other GBP, prevented viability loss, indicating that in the absence of PIM1, GBP1 was the only GBP activated in an uncontrolled manner (fig. S9D). IFN- $\gamma$ -inducible PIM1 is thus directly responsible

for phosphorylation of GBP1 on Ser<sup>156</sup>, which prevents damage to cells.

### 14-3-3 $\sigma$ -bound phospho-GBP1 is inactive

Ser<sup>156</sup> of GBP1 is part of a flexible, surface-exposed loop and is the central serine of a putative, evolutionarily conserved mode I 14-3-3 binding motif (figs. S9A and S10A). MS analysis of GBP1-interacting proteins in IFN- $\gamma$ -treated human macrophages showed the presence of all 14-3-3 proteins, including significant interactions with 14-3-3 $\beta$ ,  $\zeta$ , and  $\sigma$  (Fig. 3A and data S3), as expected (28). Immunoprecipitation of endogenous GBP1 confirmed its interaction with 14-3-3 proteins (pan-14-3-3 antibody) and with 14-3-3 $\sigma$  specifically (Fig. 3B). Immunoprecipitation of co-transfected Flag-GBP1 and hemagglutinin (HA)-tagged 14-3-3 proteins ( $\beta$ ,  $\gamma$ ,  $\epsilon$ ,  $\zeta$ ,  $\eta$ ,  $\theta$ , and  $\sigma$ ) showed promiscuous interaction of all 14-3-3 proteins with GBP1 WT but not with GBP1<sup>S156A</sup> or GBP1<sup>R153A/P158A</sup> carrying a mutated 14-3-3 binding motif (fig. S10B). The GBP1<sup>T590A</sup> mutation did not affect its binding to 14-3-3 proteins (fig. S10B). We thus further examined the potential roles of Ser<sup>156</sup> phosphorylation. The mRNA levels for the seven 14-3-3 proteins varied in human macrophages, with the abundance of 14-3-3 $\sigma$  being the lowest in naïve cells and showing an increase upon IFN- $\gamma$  treatment (figs. S6 and S10C). Expression of the other 14-3-3 family members remained unchanged (fig. S10C). Semiquantitative coimmunoprecipitations of phosphorylated endogenous GBP1 and purified HA-tagged 14-3-3 proteins corroborated our findings and showed the highest binding affinity between GBP1 and 14-3-3 $\sigma$  [dissociation constant ( $K_d$ ) =  $0.37 \pm 0.10$   $\mu$ M (SD); fig. S11]. This was independently confirmed by isothermal titration calorimetry (ITC) with recombinant 14-3-3 $\sigma$  and in vitro phosphorylated recombinant GBP1 (Fig. 3C and fig. S12). Unphosphorylated GBP1 did not bind 14-3-3 $\sigma$  (Fig. 3C), confirming its specific interaction with the phosphorylated protein.

We next reconstituted the GBP1-PIM1-14-3-3 $\sigma$  reaction in vitro and found that these proteins formed a ~125-kDa complex in the presence of ATP, most likely composed of one monomer of phosphorylated GBP1 (67 kDa) and a 14-3-3 $\sigma$  dimer (dimer: 56 kDa) (fig. S13A). The stable phospho-GBP1:14-3-3 $\sigma$  complex could be purified and analyzed by size exclusion chromatography (fig. S13B). Dimerization of GBP1 occurred in absence of GTP but increased markedly in the presence of GTP or GDP plus AlF<sub>3</sub>. The latter locks GBP1 in a GDP-bound state, showing that conformational changes in the GBP1 GTPase domain are required for its dimerization (fig. S13C). Phosphorylated and 14-3-3 $\sigma$ -bound GBP1 did not dimerize (fig. S13C). Furthermore, the rate of GTP hydrolysis by GBP1 in a GBP1:14-3-3 $\sigma$  complex was reduced by >8-fold as compared with hydrolysis

by free GBP1 (Fig. 3D). Phosphorylation of GBP1 without 14-3-3 $\sigma$  binding did not influence the rate of GTP hydrolysis (Fig. 3D).

To visualize the interaction between phosphorylated GBP1 and 14-3-3 $\sigma$ , we solved the structure of the purified protein complex (fig. S13B) using single-particle cryo-electron microscopy (cryo-EM; Fig. 3E and fig. S14 and table S1 for details). We obtained a cryo-EM map of the GBP1:14-3-3 $\sigma$  heterotrimer at 5-Å resolution, which confirmed that one 14-3-3 $\sigma$  homodimer bound to a single copy of GBP1 by grabbing its GTPase domain and interacting with the linker helix that connects the helical domain to the GTPase domain (Fig. 3E). Although the overall resolution did not permit de novo modeling, we were able to unambiguously dock previously reported crystal structures as rigid bodies based on secondary-structure features (Fig. 3E). Close interactions were observed for GBP1 loop Arg<sup>183</sup> to Thr<sup>197</sup> with the termini of helices 8 and 9 of 14-3-3 $\sigma$  copy 1. Furthermore, 14-3-3 $\sigma$  helices 5 and 9 were in contact with the parallel-running linker helix of GBP1 (Fig. 3E). In this position, the phosphate binding site of 14-3-3 $\sigma$  copy 2 was in close proximity to GBP1 Thr<sup>590</sup>, for which we also observed phosphorylation (Fig. 2F) but no effect on 14-3-3 binding upon mutation of GBP1 Thr<sup>590</sup> (fig. S10B). Thus, we hypothesize that 14-3-3 $\sigma$  binding to GBP1 functions in a similar way as 14-3-3 sequestration of Rnd3 GTPase (29), by requiring two phosphorylation sites and the farnesyl moiety. For GBP1, both Ser<sup>156</sup> and Thr<sup>590</sup> would be involved in sequential two-step 14-3-3-binding, with the initial recognition by Ser<sup>156</sup> and subsequent stabilization by binding to Thr<sup>590</sup>. In summary, our model suggests that phosphorylated GBP1 is sequestered by 14-3-3 $\sigma$ , which acts as a molecular padlock to keep the protein inactive through inhibition of dimerization and GTPase activity (Fig. 3F).

### PIM1 and 14-3-3 $\sigma$ control GBP1 activities

Having identified a role for PIM1 and 14-3-3 $\sigma$  in inhibiting the activity of GBP1, we next asked whether PIM1 and 14-3-3 $\sigma$  protected cells from the toxic effects of GBP1. We used CRISPR-Cas9 to delete 14-3-3 $\sigma$  (encoded by the gene *SFN*, also called *YWHA5*; fig. S7A) and reconstituted the cells with Dox-inducible 14-3-3 $\sigma$  (fig. S7C). Next, we measured the long-term survival of cells forced to express GBP1 mutants that cannot be recognized and inactivated by PIM1 (GBP1<sup>R151A/R153A/K155A</sup>) or 14-3-3 $\sigma$  (GBP1<sup>R153A/P158A</sup>). Similar to WT GBP1 (Fig. 1A), ectopic expression of these GBP1 mutants led to complete cell loss, pointing to their toxicity (Fig. 4A). Similar to phosphorylation-deficient GBP1<sup>S156A</sup> (Fig. 1E), IFN- $\gamma$  treatment was unable to prevent cell death (Fig. 4A). We then measured the long-term survival of WT,  $\Delta$ GBP1,  $\Delta$ PIM1,  $\Delta$ PIM1/GBP1,  $\Delta$ 14-3-3 $\sigma$ , and  $\Delta$ 14-3-3 $\sigma$ /GBP1 cells. IFN- $\gamma$  treatment

**Fig. 3. Phosphorylated GBP1 is bound and inactivated by 14-3-3 $\sigma$ .**

**(A)** Volcano plot of MS data analysis of GBP1-interacting proteins obtained after coimmunoprecipitation of Flag-GBP1 from IFN- $\gamma$  (Ctrl) or IFN- $\gamma$ - and Dox-treated THP-1 $\Delta$ GBP1+Flag-GBP1 cells. GBP1-interacting proteins above the significance threshold are highlighted in green and 14-3-3 proteins in blue.

**(B)** Immunoblots of coimmunoprecipitation of endogenous GBP1 from THP-1 WT cells treated with IFN- $\gamma$ . **(C)** ITC determining thermodynamics of GBP1:14-3-3 $\sigma$  complex formation. 14-3-3 $\sigma$  at the indicated concentrations was injected in 7- $\mu$ l aliquots to nonphosphorylated or in vitro phosphorylated GBP1 at the indicated concentrations.

The determined molar ratio  $N$  at equilibrium and dissociation constant  $K_d$  are as indicated in the figure. n.d., not determined.

**(D)** GTPase activity assay of 2  $\mu$ M free GBP1, in vitro phosphorylated GBP1, or GBP1:14-3-3 $\sigma$  complex.  $P_i$ , inorganic phosphate. **(E)** (Top) Overview of the trimeric

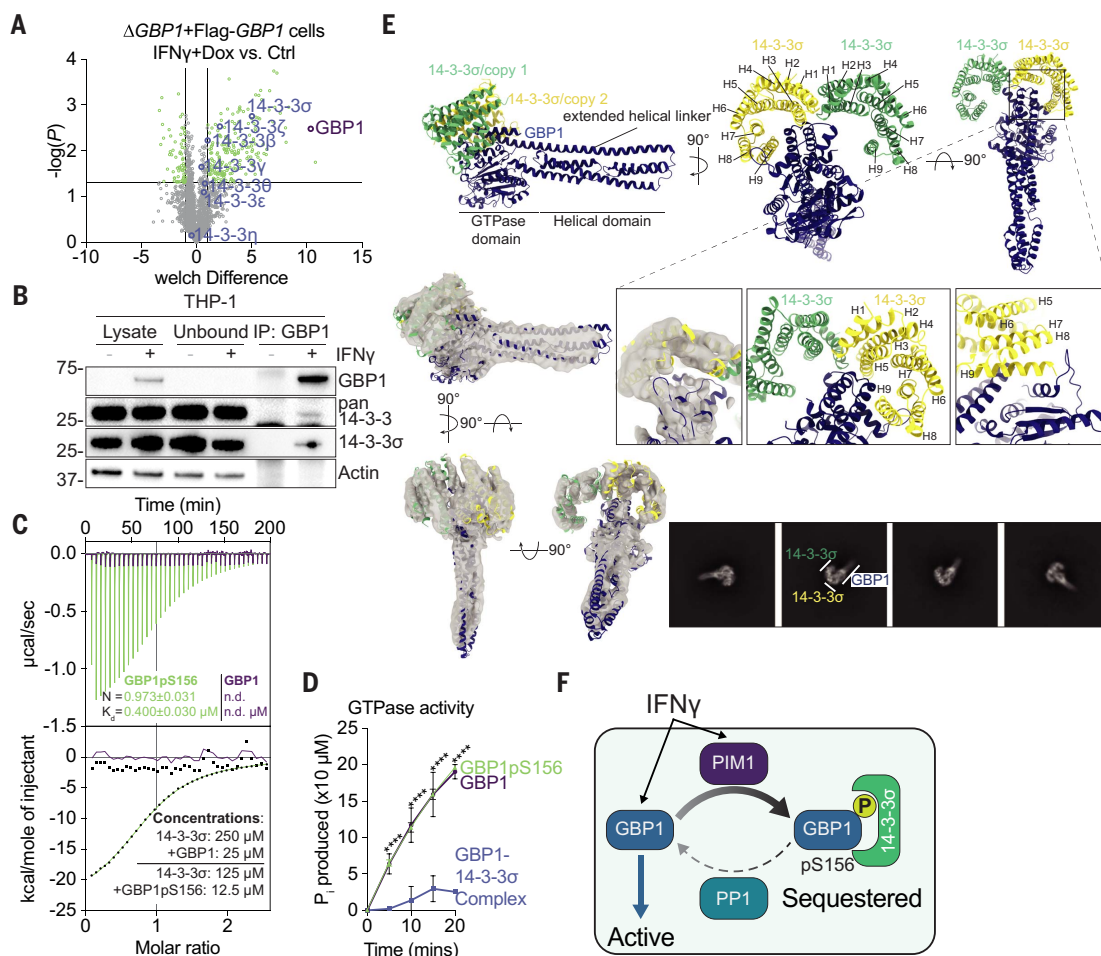
GBP1:14-3-3 $\sigma$  complex consisting of two 14-3-3 copies (yellow and green) bound to the GBP1 GTPase domain. (Middle) The insets depict details of the GBP1:14-3-3 dimer binding interface. The cryo-EM density is shown in gray with rigid-body docked GBP1 [Protein Data Bank (PDB) ID 1F5N] and 14-3-3 $\sigma$  (PDB ID 1YWT) crystal structures. (Bottom) Representative 2D classes with highlighted complex components. H, helix. **(F)** Graphic depicting the observed inhibitory mechanism, in which PIM1 phosphorylates human GBP1 at Ser<sup>156</sup>,

of  $\Delta$ PIM1 cells led to cell loss, as previously observed (Fig. S9D), as did IFN- $\gamma$  treatment of  $\Delta$ 14-3-3 $\sigma$  cells (Fig. 4B). In both cases, cell loss was prevented by additional knockout of GBP1, whereas IFN- $\gamma$  treatment of THP-1 WT or  $\Delta$ GBP1 cells did not reduce viability (Fig. 4B). Moreover, both GBP1 mutants and endogenous GBP1 in  $\Delta$ PIM1 or  $\Delta$ 14-3-3 $\sigma$  cells were prone to dimerization (Fig. 4C) and localization to cellular membranes in IFN- $\gamma$ -exposed macrophages (Fig. 4D). Again, this resembled the phosphorylation-deficient S156A mutant (Fig. 1, F and G).

To test whether this mechanism holds true at the tissue level, we used IFN- $\gamma$ -responsive, patient-derived colorectal tumor organoids and tested whether the GBP1:PIM1 interaction inhibitor NSC756093 affected cell viability, organoid growth, and stemness. IFN- $\gamma$  treatment alone had no impact on organoid

survival or growth, and the inhibitor NSC756093 alone only caused mild cytotoxicity (Fig. 4E). However, treatment with a combination of IFN- $\gamma$  and inhibitor (thereby unleashing GBP1 from its phosphorylation-driven control) decreased organoid growth by ~60% over the course of 4 days (Fig. 4E). We confirmed these findings by visual inspection, observing fewer and smaller organoids upon treatment with IFN- $\gamma$  and NSC756093 compared with untreated or IFN- $\gamma$ - or inhibitor-only treated samples. (Fig. 4F). To further interrogate the effects of treatment with IFN- $\gamma$  and NSC756093, we next evaluated the stemness of organoids using stem-forming assays. To do so, organoids pretreated with IFN- $\gamma$  and NSC756093 for 48 hours were dissociated, reseeded, and left to grow back into organoids for 7 days without any additional treatment (Fig. 4, G and H). This revealed a lasting effect of IFN- $\gamma$  and NSC756093

which is subsequently bound by 14-3-3 $\sigma$ . Upon dephosphorylation, GBP1 is liberated and becomes active. Data information: Images in (B) are representative of  $n = 3$  experiments. Graphs in (A) and (D) show mean  $\pm$  SD from  $n = 3$  experiments. Curves in (C) are representative of  $n = 3$  experiments and fitted to a model with one set of binding sites. \*\*\*\* $P < 0.0001$  for indicated comparisons in (D) from two-way ANOVA after adjustment for multiple comparisons. For gel source data, see data S5.



on the ability of organoid precursors to self-renew and illustrates the potency of GBP1 in colorectal tumor organoids (Fig. 4, G and H). In summary, PIM1 and 14-3-3 $\sigma$  are required to control the activity of GBP1 in human cells by phosphorylation and cytosolic sequestration.

### Toxoplasma infection depletes PIM1 and activates GBP1

We hypothesized that in the absence of phosphorylation of GBP1 by PIM1 and its sequestration by 14-3-3 $\sigma$ , GBP1 is free to target pathogen compartments more effectively. To test how control of GBP1 affects its trafficking and antimicrobial activities, we quantified its ability to restrict growth of Tg. We tested cells that expressed GBP1 mutants with impaired phosphorylation (S156A and R151A/R153A/K155A) or binding of 14-3-3 $\sigma$  (R153A/P158A), cells that lacked PIM1 (or expressing kinase-dead PIM1<sup>P81S</sup>), and



#### Fig. 4. PIM1 phosphorylation of GBP1 protects cells from self-inflicted damage.

(A) XTT cell survival assay of THP-1ΔGBP1+GBP1 WT, THP-1ΔGBP1+GBP1<sup>R151A/R153A/K155A</sup> (kinase motif mutant), or THP-1ΔGBP1+GBP1<sup>R153A/P158A</sup> (14-3-3 binding motif mutant) cells treated with IFN-γ with or without Dox for the indicated number of days.

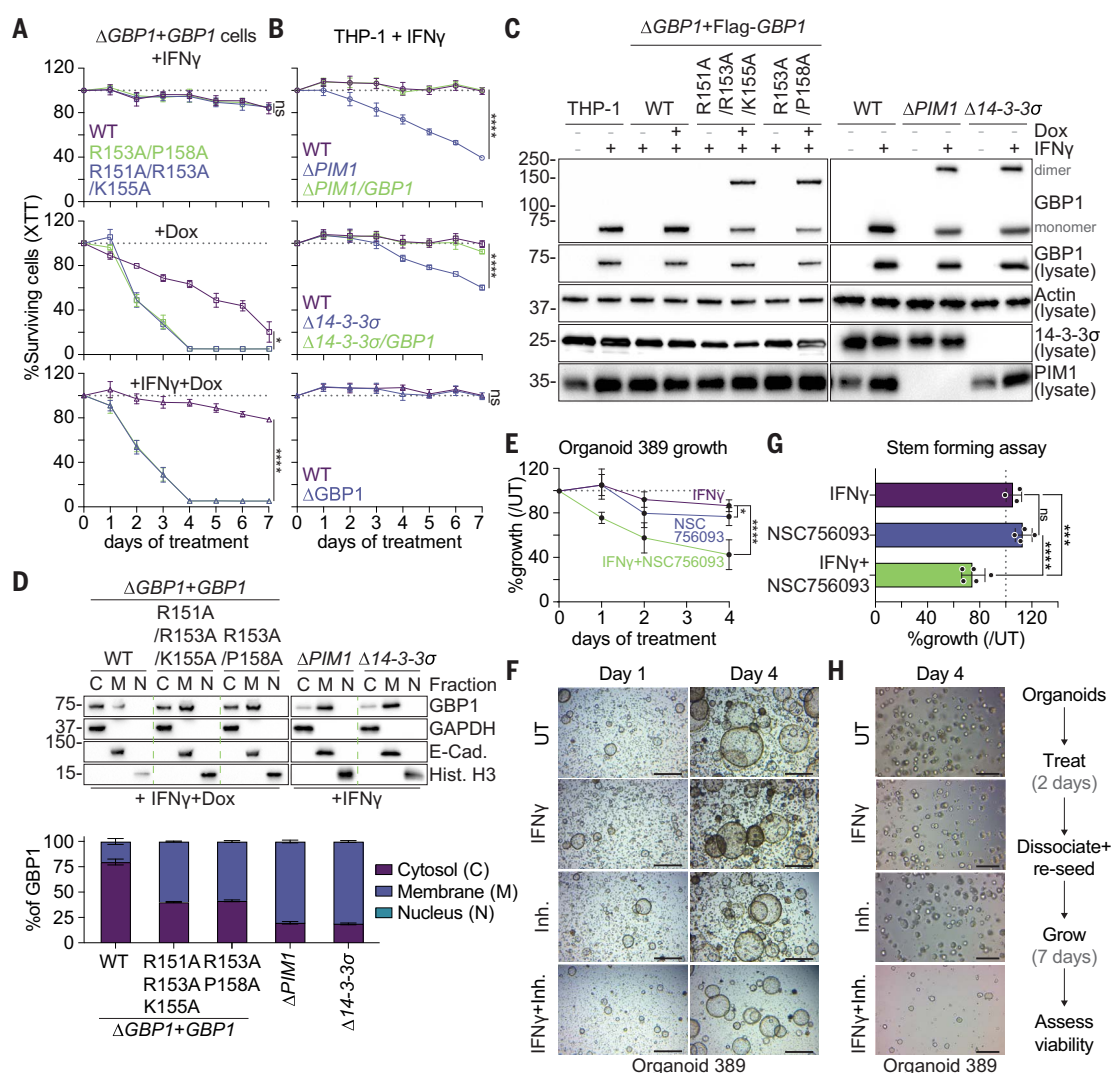
(B) XTT cell survival assay kinetics of THP-1ΔGBP1, ΔPIM1, Δ14-3-3σ, ΔPIM1/GBP1, or Δ14-3-3σ/GBP1 cells treated with IFN-γ for the indicated number of days.

(C) Immunoblot analysis of GBP1 in cross-linked pellets and in cell lysates of indicated cells treated with IFN-γ with or without Dox or left untreated.

(D) Immunoblots of subcellular fractionation to determine GBP1 localization in indicated cells with respective markers for the cytosol (C), membranes (M), or the nucleus (N) (top) and quantification of localization (bottom).

(E) MTT survival assay of patient-derived colorectal tumor organoids treated with IFN-γ and NSC756093 for 4 days, shown as percent growth compared with untreated (UT) controls.

(F) Bright-field microscopy images of organoids after the indicated treatments with IFN-γ and inhibitor NSC756093 (Inh.). Scale bars are 1 mm. (G) Stem-forming assay of organoids treated for 2 days as indicated, dissociated, and regrown for 7 days in the absence of treatment. The graph shows the results of MTT assays on day 7 after reseeded. (H) Representative bright-field microscopy images from day 4 of regrowth of the stem-forming assay. Scale bars are 200 μm. Data information: Images in (C) and (D) and (F) to (H)



cells that lacked 14-3-3σ. All displayed increased recruitment of GBP1 to Tg vacuoles, restricted the growth of Tg more efficiently, and showed increased disruption of Tg-containing vacuoles and parasites, with a subsequent higher induction of apoptosis as compared with IFN-γ-treated THP-1 WT controls (Fig. 5A). These results indicate increased parasitocidal activity of GBP1 in conditions that prevent GBP1 phosphorylation and/or its interaction with 14-3-3σ. Reconstituting knockout cells with either WT PIM1 or 14-3-3σ decreased all pathogen control measures back to THP-1 WT levels (Fig. 5A).

When assessing the dynamics of the association of GBP1 with Tg-containing vacuoles, GBP1 was recruited faster and to higher levels

in both ΔPIM1 and NSC756093-treated THP-1 WT cells (fig. S15, A and B). Fluorescence recovery after photobleaching assays (FRAP) showed increased mobility of mCh-tagged GBP1 in ΔPIM1 cells or cells that express mCh-GBP1<sup>S156A</sup>, which could explain the faster kinetics of GBP1 recruitment to Tg vacuoles (fig. S15C). Conversely, the silencing of *PPP1CA* impaired the growth control of Tg, whereas treatment with NSC756093 improved it. Depletion of PIM2 or PIM3 affected neither GBP1 recruitment to Tg vacuoles nor growth control of Tg (fig. S15, D to F).

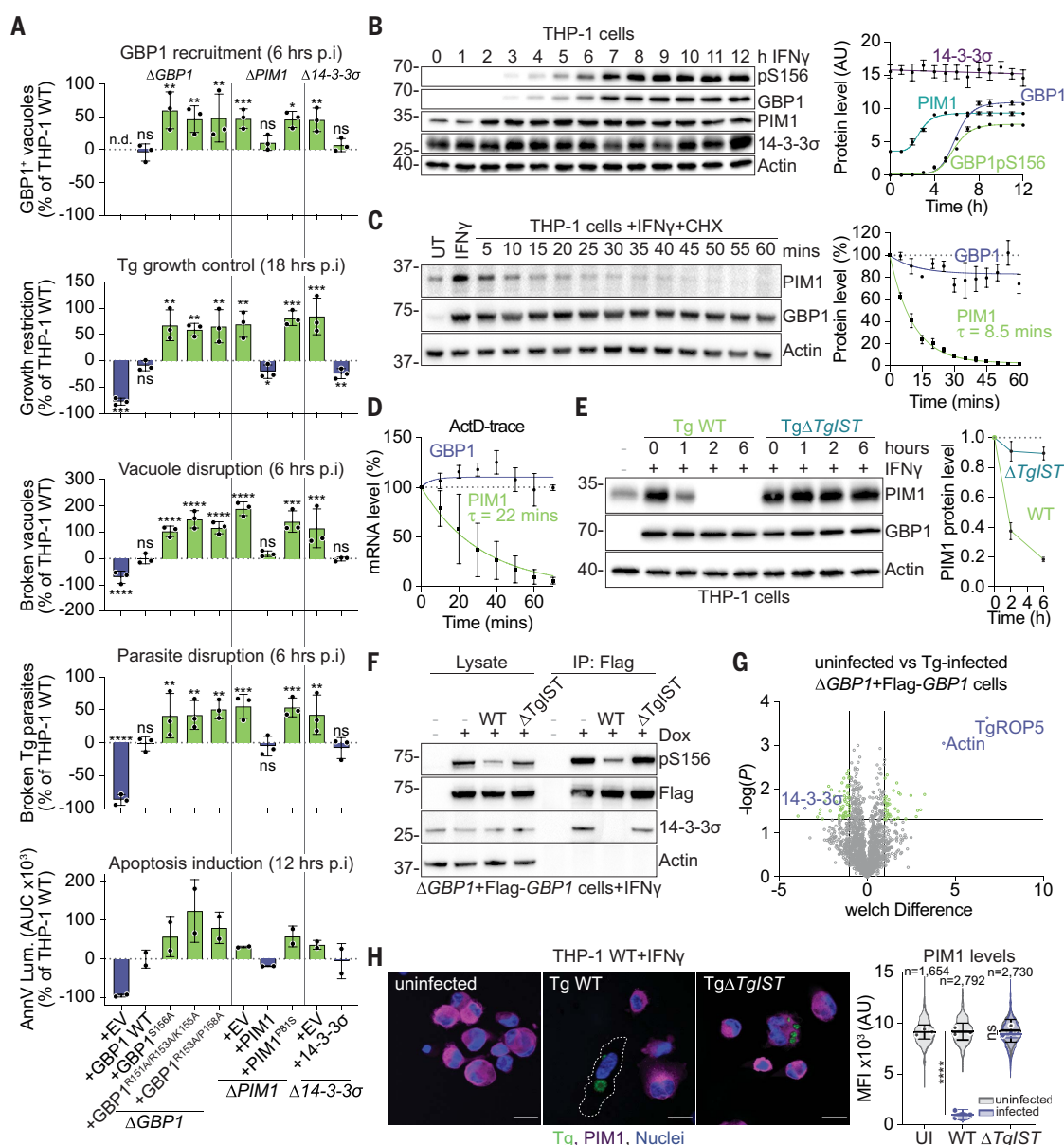
We next sought to determine how GBP1 phosphorylation and protein abundance changed in Tg-infected cells. We first measured the induction of GBP1, 14-3-3σ, and PIM1 as well as the

are representative of  $n = 3$  experiments. Graphs in (A), (B), (D), (E), and (G) show mean  $\pm$  SEM from  $n = 3$  experiments, normalized to untreated cells. \* $P \leq 0.05$ , \*\*\* $P \leq 0.001$ , and \*\*\*\* $P \leq 0.0001$  in (A), (B), and (E) comparing all conditions with WT or untreated cells and for indicated comparisons in (E) and (G) from one-way ANOVA; ns is not significant. For gel source data, see data S5.

appearance of Ser<sup>156</sup>-phosphorylated GBP1 in THP-1 WT cells after IFN-γ treatment (Fig. 5B). This time course showed a more rapid induction of PIM1 than GBP1. Contrary to our RT-qPCR data (fig. S10C), these results showed that the levels of 14-3-3σ did not change (Fig. 5B). Notably, GBP1 appeared to be phosphorylated soon after it was expressed (Fig. 5B), indicating that the PIM1 and 14-3-3σ-mediated control of GBP1 was immediately active. PIM1 protein and mRNA were unstable and short-lived [half-life ( $\tau_{1/2}$ ) ~8.5 or ~22 min, respectively] as compared with the more-stable GBP1 (protein  $\tau_{1/2} > 12$  hours; Fig. 5, C and D). This led us to hypothesize that PIM1 degradation might serve to uncouple the inhibition of GBP1. In this way,

**Fig. 5. *Toxoplasma* infection depletes PIM1 and activates GBP1.**

**(A)** Quantification of GBP1 recruitment to Tg vacuoles, Tg growth restriction, vacuole and parasite disruption, and apoptosis assay [area under the curve (AUC)] in IFN- $\gamma$ - and Dox-treated cells expressing the indicated mutant of GBP1,  $\Delta$ PIM1 cells, or  $\Delta$ 14-3-3 $\sigma$  cells reconstituted with the indicated protein or empty vector (EV). Values plotted relative to IFN- $\gamma$ -primed WT cells. n.d., not detected; p.i., postinfection. **(B)** Immunoblots of IFN- $\gamma$ -treated THP-1 WT cells (left) and protein level quantification (right). **(C)** Immunoblots of THP-1 WT cells treated with 50  $\mu$ g/ml cycloheximide (CHX) (left) and quantification of protein half-life (right). **(D)** RT-qPCR determination of mRNA stabilities in THP-1 WT cells treated with actinomycin D (ActD). **(E)** Immunoblots (left) and quantification (right) of PIM1 protein levels in THP-1 WT cells treated with IFN- $\gamma$  and infected with Tg WT or  $\Delta$ Tg/ST. **(F)** Immunoblots of Flag-GBP1 coimmunoprecipitation from IFN- $\gamma$ - and Dox-treated THP-1  $\Delta$ GBP1+Flag-GBP1 cells infected with Tg WT or  $\Delta$ Tg/ST for 6 hours. **(G)** MS analysis of GBP1-interacting proteins in uninfected or Tg WT-infected and IFN- $\gamma$ - and Dox-treated THP-1  $\Delta$ GBP1+Flag-GBP1 cells. **(H)** Immunofluorescence images (left) of IFN- $\gamma$ -primed and uninfected or Tg WT- or  $\Delta$ Tg/ST-infected THP-1 WT cells after 12 hours. Scale bars are 20  $\mu$ m. Dashed white line, cell outline; magenta, PIM1; green, Tg; blue, nuclei. The graph (right) shows quantification of PIM1 mean fluorescence intensity (MFI) depending on infection status. Gray, uninfected cells; blue, infected cells. Data information: Images in (B), (C), (E), (F), and (H) are representative of  $n = 3$  experiments. Graphs in (A) show



mean  $\pm$  SD of  $n = 3$  experiments. Graphs in (B) and (C) show mean  $\pm$  SD from  $n = 3$  experiments, and graphs in (D) and (E) show mean  $\pm$  SD from  $n = 4$  experiments. Graphs in (G) show data from  $n = 3$  replicates. \* $P \leq 0.05$ , \*\* $P \leq 0.01$ , \*\*\* $P \leq 0.001$ , and \*\*\*\* $P \leq 0.0001$  in (A) from two-way ANOVA comparing all conditions with THP-1 WT cells and in (H) from nested  $t$  test comparing infected with uninfected cells after adjustment for multiple comparisons; ns is not significant. For gel source data, see data S5.

IFN- $\gamma$ -induced PIM1 serves a dual role: It functions as a guard that detects pathogen-mediated interference of IFN- $\gamma$  signaling (leading to depletion of PIM1), and it protects self-membranes from damage inflicted by GBP1. Tg secretes a pathogen effector protein called *T. gondii* inhibitor of STAT1 transcriptional activity (TgIST). Upon entering the host cell nucleus, TgIST sequesters STAT1 on specific loci and facilitates the formation of nonpermissive chromatin by recruiting the nucleosome remodeling deacet-

ylase (NuRD) repressor complex. The nascent transcription sites thereby remain silenced (30, 31). Given the IFN- $\gamma$ -inducible nature of the *PIM1* gene, we hypothesized that TgIST completely shuts down *PIM1* gene expression, leading to the loss of PIM1. Indeed, we observed rapid TgIST-dependent depletion of PIM1 upon infection with Tg (Fig. 5E), further precipitating the loss of GBP1 phosphorylation and interaction with 14-3-3 $\sigma$  (Fig. 5F). MS of GBP1 interactomes of Tg-infected cells confirmed

decreased interaction of GBP1 with 14-3-3 $\sigma$  and showed increased interaction with host-derived actin and parasite-derived TgROP5 compared with uninfected cells (Fig. 5G and data S4). These experiments show that the activity of GBP1 is restrained in uninfected cells but can be rapidly triggered upon infection by a pathogen that interferes with IFN- $\gamma$  signaling. Supporting our hypothesis of bystander cell protection, we found that PIM1 was depleted specifically only in Tg WT-infected macrophages



but not in uninfected cells from that same experiment or in  $\Delta TgIST$ -infected cells (Fig. 5H).

Finally, we wanted to investigate the effect of PIM1 and 14-3-3 $\sigma$  on GBP1 activity against Gram-negative bacteria such as *Salmonella* Typhimurium (STm), which is distinct from its activity against vacuolar pathogens such as Tg. For comparison, we assessed the cellular distribution of PIM1, 14-3-3 $\sigma$ , GBP1, and Ser<sup>156</sup>-phosphorylated GBP1 in cells infected with Tg or STm by immunofluorescence imaging (fig. S16). In uninfected cells, all proteins showed a high degree of colocalization (Pearson's coefficient >0.88; fig. S16A). In Tg-infected cells, we observed the rapid recruitment of GBP1 to Tg vacuoles but no recruitment of PIM1, 14-3-3 $\sigma$ , or GBP1pS156 (GBP1 phosphorylated at Ser<sup>156</sup>) (fig. S16B). This corroborated our finding that GBP1 must be dephosphorylated and released from sequestration before acquiring its parasitocidal, pathogen-proximal activity. We also observed decoration of the bacterial surface of cytosolic STm by GBP1 alongside recruitment of PIM1, 14-3-3 $\sigma$ , and GBP1pS156 (fig. S16C), suggesting that GBP1's high-affinity to LPS might override control by PIM1-mediated phosphorylation and 14-3-3 $\sigma$  sequestration. Supporting this finding, we did not observe degradation of PIM1 or dephosphorylation of GBP1 upon STm infection (fig. S16D). Finally, in  $\Delta 14-3-3\sigma$  cells, phosphorylated GBP1 was recruited to Tg vacuoles, demonstrating that retention by 14-3-3 $\sigma$  in the cytosol, not phosphorylation by PIM1 alone, ultimately controlled GBP1 pathogen-compartment targeting (fig. S16E).

## Discussion

Human GBP1 is a membrane-active large GTPase that can disrupt microbe-encapsulating membranes (5–15). However, GBP1 can also associate with the Golgi apparatus (16, 20) and/or the plasma membrane (13, 16). How GBP1 activity is regulated in cells and how it is recruited to specific subcellular sites has remained elusive. In this work, we found that a large fraction of GBP1 is phosphorylated by the kinase PIM1 at Ser<sup>156</sup>, establishing that posttranslational modification of human GBP1 regulates its activity. Ser<sup>156</sup>-phosphorylated GBP1 was sequestered in the cytosol by 14-3-3 $\sigma$ , thereby preventing self-inflicted damage, in a mechanism reminiscent of how Rnd3 GTPase is inactivated (29). Thus, IFN- $\gamma$ -exposed macrophages are in an activated state but keep GBP1 on standby and its activity tightly controlled. In uninfected cells, ectopic expression and unrestrained action of GBP1 led to necrosis. Similarly, ectopic expression of GBP1 in ovarian cancer cells reduces their viability by ~25% within 3 days (32). In infected cells, the Tg-induced block of IFN- $\gamma$  signaling-induced transcription depletes inherently short-lived PIM1 (33) and springs a trap that unleashes GBP1 onto the pathogen-containing compartment. Pathogens from all

kingdoms of life have evolved effector proteins that interfere with the integrity of IFN- $\gamma$  signaling. Some examples include *Mycobacterium tuberculosis* blocking transcriptional transactivation downstream of STAT1 (34), *Vaccinia virus* phosphatase H1 targeting STAT1 for dephosphorylation (35), human cytomegalovirus depleting JAK kinases (36), and hepatitis C virus NS5A protein or *Leishmania donovani* both disrupting STAT1 phosphorylation (37, 38). The cytokine-induced kinase PIM1 may thus serve as a detector for a broad range of pathogens that interfere with IFN- $\gamma$  signaling. Consistent with our work, PIM1 is a host factor that favors survival of Tg (39, 40). Furthermore, PIM1 is a known GBP1-interacting protein in cancer cells (21) and is a prosurvival proto-oncogene that negatively regulates other proapoptotic proteins (24, 26, 41–44). Given GBP1's ability to promote programmed cell death, use of the specific GBP1:PIM1 interaction inhibitor (21) is a promising way to chemically activate GBP1, with implications for innate immunity and cancer therapy.

Innate immune mechanisms that can cause cellular damage must be carefully regulated to ensure protection of bystander cells. The activity of immune effectors is tightly controlled, either indirectly through inactivation of inhibitory guard proteins or directly through activation of upstream PRRs. The indirect guard mechanisms, originally described in plants (45), detect the interference of pathogens with key cellular processes, whereas the direct PRR mechanisms respond to conserved pathogen-associated molecular patterns. An example of such “guarding” in Mammalia that is conceptually similar to the inactivation of GBP1 is the regulation of the Pyrin inflammasome, whereby the cytoskeleton-sensing kinases PKN1 and 2 phosphorylate Pyrin and inactivate the protein through the binding of 14-3-3 proteins. This system relays microbial perturbation of the cytoskeleton and thereby indirectly triggers immunity (46–49). Other recent examples include “self-guarding” of MORC3, which controls HSV-1 infection and secondary type I IFN responses (50), or viral disruption of protein synthesis that triggers apoptosis through the depletion of short-lived BCL-2 protein family members (51). Given the short half-life of PIM1, it is tempting to speculate that translation inhibition might also unleash GBP1 from its restriction. GBP1 directly activates immunity through its bona fide PRR function for cytosolic LPS (7, 11, 13–15). As we found in this work, its other, parasitocidal function is controlled by PIM1. Thus, GBP1 combines both innate immune surveillance strategies and antimicrobial activity in a single effector protein. The integration of an IFN- $\gamma$ -induced pathway with posttranslational control of innate immune defense could cover a broad range of pathogens and enable cells to autonomously regulate immunity depending on their infection

status. Similar cytokine-induced guard circuitries are likely to exist and thus ensure the protection of innocent bystander cells.

## Materials and methods

### Cell, parasite, and bacteria culture, infections, and treatments

THP-1 cells (TIB202, ATCC) were maintained in Roswell Park Memorial Institute (RPMI) medium with GlutaMAX (35050061, Gibco) supplemented with 10% fetal bovine serum (FBS) (Sigma), at 37°C in 5% CO<sub>2</sub>. THP-1 cells were differentiated with 50 ng/ml phorbol 12-myristate 13-acetate (PMA) (P1585, Sigma) for 3 days and left to rest for 2 days by replacing the differentiation medium with complete medium without PMA. Human embryonic kidney 293T (HEK293T) cells (Cell Services, The Francis Crick Institute, London, UK), NIH3T3 cells (CRL-1658, ATCC), and human foreskin fibroblasts (HFFs) (SCRC-1041, ATCC) were cultured in Dulbecco's modified Eagle's medium (DMEM) with GlutaMAX (Gibco) supplemented with 10% FBS (Sigma) at 37°C in 5% CO<sub>2</sub>. Cells were not used beyond passage 25 and HFFs not beyond passage 15.

Patient-derived colorectal tumor organoids (Organoid 389), originally derived from a T3N1 poorly differentiated, mismatch repair-proficient adenocarcinoma of the sigmoid colon from a male subject (52), were grown and maintained in 50  $\mu$ l of Matrigel domes (CLS356231, Corning) with 500  $\mu$ l of human IntestiCult medium (06010, StemCell) in 24-well plates at 37°C and 5% CO<sub>2</sub> and passaged weekly.

Tg were maintained by serial passage on HFF cells that were cultured in DMEM with GlutaMAX supplemented with 10% FBS at 37°C in 5% CO<sub>2</sub>. Parasites were passaged the day before infection to maintain high viability. Tg were prepared from freshly 25-gauge-syringe-lysed HFF cultures by centrifugation at 50g for 3 min; the cleared supernatant was transferred into a new tube and followed by subsequent centrifugation at 500g for 7 min and resuspension of the pelleted parasites into fresh complete medium. Parasites were added to the cells at a multiplicity of infection (MOI) of 1. Infection was synchronized by centrifugation at 500g for 5 min. Two hours after infection, extracellular parasites were removed with three washes using warm phosphate-buffered saline (PBS) (806552, Sigma), and fresh complete medium was added before culturing at 37°C and 5% CO<sub>2</sub> for the required time.

STm strain SL1344-GFP (GFP, green fluorescent protein) (11) was maintained under ampicillin selection (11593027, Gibco) and grown on LB plus ampicillin agar plates. One day before infection, bacteria from a single colony were inoculated and grown overnight at 37°C. The overnight culture was diluted 1:20 into LB plus 300 mM NaCl and grown with shaking in a closed container to an optical density at 600 nm (OD<sub>600</sub>) of 0.9. Bacteria were harvested

by centrifugation at 1000g for 5 min, washed with serum-free cell culture medium twice, and resuspended in 1 ml of plain medium. Cells were infected with STm at an MOI of 10, and infections were synchronized by centrifugation at 750g for 10 min. Infected cells were washed three times with warm PBS 30 min after infection, and fresh medium containing 10 µg/ml gentamicin (15750060, Gibco) was added. The bacterial MOI used for infections was confirmed by plating on LB agar plates. An overview of all cell lines, parasites, and bacteria strains can be found in table S2. All cell culture work was performed without the addition of antibiotics, and the cells were regularly tested for mycoplasma contamination by immunofluorescence and PCR.

THP-1 cells were stimulated for 16 hours before infection in complete medium with addition of 50 international units (IU)/ml human IFN-γ (285-IF, R&D Systems). Induction of protein expression in the Dox-inducible cells was performed with 200 ng/ml Dox (D9891, Sigma) overnight. To block translation for studying protein stability, cells were treated with 50 µg/ml cycloheximide (CHX) (C7698, Sigma), and to block transcription, cells were treated with 6 ng/ml actinomycin D (A1410, Sigma). To block the GBP1:PIM1 interaction, cells were treated with 100 nM NSC756093 (SML1310, Sigma). For in vitro assays, NSC756093 was used at 1 µM. To chemically induce pyroptosis, cells were primed with 100 ng/ml LPS O111:B4 (NC9673121, Enzo) and subsequently treated with 10 µM nigericin. Treatments to induce apoptosis were performed with 50 ng/ml tumor necrosis factor-α (TNFα) (210-TA, R&D Systems) and 10 µg/ml CHX. The pan-caspase inhibitors zVAD-fmk (25 µM, 60332, Cell Signaling Technologies) or qVD (20 µM, ab141421, Abcam) were used to block caspase activation for necroptosis induction or blocking apoptosis or pyroptosis. To inhibit pyroptosis, cells were treated with 10 µM Mcc950 (inh-mcc, InvivoGen) or 50 µM disulfiram (DSF) (1224008, Sigma). To inhibit necroptosis, cells were treated with 50 µM GSK'872 (6492, Tocris) or 10 µM necrosulfonamide (NSA) (5025, Tocris). Tumor organoid cultures were treated with 100 IU/ml IFN-γ or 1.66 µM NSC756093.

#### Plasmid DNA and siRNA transfection

THP-1 cells were transfected with 30 nM siRNAs 2 days before infection (table S3). The transfection mix was prepared as a 10× mix in OptiMEM containing the siRNA(s) and TransIT-X2 transfection reagent (MIR600x, Mirus) in a 1:2 ratio. All siRNAs were ON-TARGETplus pools from Dharmacon, with the negative control being ON-TARGETplus Non-targeting Pool (D-001810, Dharmacon). Transfection of DNA plasmids was performed using Lipofectamine 2000, following the manufacturer's instructions (11668027, Invitrogen).

#### Lentiviral transduction

Lentiviral packaging used HEK293T cells transfected with equimolar ratios of the required expression plasmid, pMD2.G, and psPAX2 (Addgene, 12259 and 12260, respectively, both gifts from D. Trono) using Lipofectamine 2000 in serum-free DMEM. Medium was replaced 12 hours after transfection with fresh DMEM plus 10% FBS to rest the cells and again after 12 hours with DMEM plus 10% FBS containing 5 mM sodium butyrate (B5887, Sigma). The next day, medium was replaced with RPMI medium plus 10% FBS, and the cells were left to produce lentiviral particles for 1 day. Virus containing supernatant was filtered through a 0.43-µm syringe filter and supplemented with 8 µM polybrene (H9268, Sigma). The target cells were then resuspended in 500 µl of the virus-containing medium and "spininfected" for 30 min at 1000g. One hour after infection, 1 ml of complete medium was added, and the cells were left to rest. The infection procedure was repeated a total of three times before selection with the appropriate selection reagent: 1 µg/ml puromycin (A1113802, Gibco), 200 µg/ml zeocin (J67140, Alfa Aesar), and/or 15 µg/ml blasticidin S (15205, Sigma). Once untransduced control cells had died in the selection medium, the newly created cells were verified for successful transduction by immunoblotting.

#### Creation of new cell lines

##### Inducible GBP1 cell lines

THP-1ΔGBP1, THP-1ΔGBP1+Tet-GBP1 WT, THP-1ΔGBP1+Tet-Flag-GBP1 WT, and THP-1ΔGBP1+Tet-mCH-GBP1 WT have been published before, and new cell lines were created identically using lentiviral transductions (11). To make cells expressing mutated GBP1, pLenti-Tet-GBP1 plasmids (11), with and without tags, were mutated using site-directed mutagenesis and transduced into the THP-1ΔGBP1+Tet target cells using lentiviral transduction as described before.

##### PIM1 and 14-3-3σ (SFN/YWHAS) CRISPR knockout cells

Guide RNA (gRNA) sequences targeting the 5' and 3' untranslated regions (UTRs) of the respective genes were designed using the MIT CRISPR design tool (crispr.mit.edu) (table S4). DNA oligonucleotides encoding the CRISPR RNA (crRNA) were annealed and cloned into BsmBI-digested (ER0451, Thermo Fisher Scientific) pLentiCRISPR-V2 backbone (53) using Quick Ligation kit (M2200, New England Biolabs) and transduced into THP-1 WT or THP-1ΔGBP1 cells using lentiviral particles. After selection with puromycin for 7 days, cells were subcloned by serial dilution into 96-well plates using preconditioned complete medium supplemented with nonessential amino acids (11140076, Gibco), penicillin and streptomycin, and GlutaMAX. Roughly 3 weeks after seeding, obtained clones were expanded and screened

for the absence of target protein expression by RT-qPCR. Clones that showed reduced or absent target protein expression underwent secondary screening by immunoblotting. For each of the cell lines, >4 single-cell clones with confirmed absence of either PIM1 or 14-3-3σ protein were pooled and cultured for 2 more weeks before undergoing final screening to confirm absence of the proteins. This resulted in the THP-1ΔPIM1, ΔPIM1/GBP1, Δ14-3-3σ, and Δ14-3-3σ/GBP1 cell lines.

#### Reconstitution of PIM1 and 14-3-3σ

CRISPR knockout cells of PIM1 and 14-3-3σ were transduced with the Dox-inducible system as previously described (11). To create PIM1- and 14-3-3σ-expressing Dox-inducible plasmids (pLenti-Tet-PIM1 or pLenti-Tet-14-3-3σ), the empty vector backbone was digested with BamHI, PIM1 and 14-3-3σ open reading frames (ORFs) were amplified from cDNA obtained from IFN-γ-primed THP-1 WT cells, and all fragments assembled with Gibson assembly. Further, the pLenti-Tet-PIM1 plasmid was mutated by site-directed mutagenesis to obtain a pLenti-Tet-PIM1<sup>PSIS</sup> kinase-dead version, and all vectors transduced into the respective target cells using lentiviral transduction.

#### RT-qPCR

RNA was extracted from  $0.25 \times 10^6$  cells using Trizol reagent (15596026, Invitrogen). GlycoBlue (5 µg/ml, AM9516, Invitrogen) was added during the isopropanol precipitation step. RNA quality was measured on a Nanodrop 2000 Spectrophotometer (Thermo Fisher Scientific). One microgram of RNA was reverse transcribed using a high-capacity cDNA synthesis kit (4368813, Applied Biosystems). For qPCR, the PowerUP SYBR green kit (A25742, Applied Biosystems), 20 ng cDNA in a 10-µl reaction, and primers at 1 µM final concentration (sequences in table S5) were used. Primer specificity was ensured by designing primers to span exon-exon junctions, whenever possible, and for each primer pair, a melt curve was recorded and compared with in silico predicted melt curves from uMelt (54) and amplicon sizes were analyzed by agarose gel electrophoresis. Recorded cycle threshold (Ct) values were normalized to the recorded Ct of human *HPRT1*, and data were plotted as ΔCt (relative expression). To determine absolute expression, defined amounts of linearized plasmid standards were used as PCR template and the obtained Ct values used to calculate transcript numbers.

#### MTT, XTT, and AnnV glow assays for cell survival and death

To determine cell viability using XTT assays (Cell Proliferation Kit II, Roche), 25,000 cells were seeded per well in a 96-well plate or 10,000 cells in a 384-well plate and differentiated as described before. Cells were treated in RPMI



without phenol red (11835, Gibco). The detection reagent was freshly prepared according to the manufacturer's instructions and added before the viability determination. Cells were then incubated at 37°C for 4 hours, and absorbance was measured at 475 and 660 nm for correction.

For organoid growth analysis, MTT reagent (M6494, Invitrogen) was added in a 1:10 dilution to the plates, and the Matrigel domes were disrupted by pipetting. Plates were returned to a 37°C incubator for 30 min before adding lysis solution (4 mM HCl, 0.1% Triton-X100 in isopropanol), mixing by pipetting, and placing on a shaker in the dark for 10 min. Each well was thoroughly mixed, lysates were transferred in quadruplicates to a microplate, and absorbance was read at 550 nm on an iMark Microplate Absorbance Reader (Bio-Rad). Medium with Matrigel was used as a negative control.

Apoptosis kinetics were analyzed using the RealTime-Glo Annexin V Apoptosis Assay (JA1001, Promega) according to the manufacturer's instructions. In brief, 50,000 cells were seeded per well of a white, tissue culture-treated 96-well plate, differentiated, pretreated, and infected. Simultaneously with infection, detection reagent was added. Luminescence was measured using a Fluostar Omega plate reader (BMG Labtech) that was preheated to 37°C. No-cell, medium-only controls were used for background correction. To determine overall cell death levels, the area under the curve (AUC) was determined using Prism 8.4 (GraphPad, Inc.).

#### Molecular cloning of vectors for transient expression

For transient expression of Flag-GBP1 after transfection, the ORF was amplified by PCR using Q5 polymerase and cloned into BamHI- and EcoRI-digested pcDNA3.1(+) vector using the Quick Ligation kit. pcDNA3-HA-14-3-3 $\beta$ ,  $\gamma$ ,  $\epsilon$ ,  $\zeta$ , and  $\sigma$  were a gift from A. Ridley (University of Bristol, Bristol, UK) (29) and M. Yaffe (MIT, Boston, MA, USA) (55). To produce N-terminally HA-tagged 14-3-3 $\eta$  and 14-3-3 $\theta$  in a pcDNA3 vector identical to the other constructs, the pcDNA3-HA backbone was amplified by PCR. 14-3-3 $\eta$  was amplified from pCS2-HA-14-3-3 $\eta$  (Addgene, 116887, a gift from F.-Q. Li and K.-I. Takemaru) (56) and 14-3-3 $\theta$  from pcDNA3-14-3-3 $\theta$ -HA (a gift from A. Ridley), and finally, inserts and backbone were assembled by Gibson assembly.

#### SDS-PAGE, immunoblotting, and gel staining

For immunoblotting,  $0.5 \times 10^6$  cells were seeded per well of a 48-well plate, differentiated with PMA, pretreated, and infected as described above. At the end of treatments, cells were washed with ice-cold PBS and lysed for 5 min on ice in 50  $\mu$ l of RIPA buffer (150 mM NaCl, 1% Nonidet P-40, 0.5% sodium deoxycholate, 0.1% SDS, 25 mM Tris-HCl pH 7.4) supplemented with protease inhibitors (Protease Inhibitor Cocktail set III, EDTA free, Merck) and PhosSTOP phosphatase inhibitors (4906845001,

Roche). Lysates were cleared by centrifugation at full speed for 15 min at 4°C. Subcellular fractionation was performed using the QProteome Cell Compartment Kit (37502, Qiagen) following the manufacturer's instructions. Bicinchoninic acid (BCA) assay (Pierce BCA protein assay kit, 23225, Thermo Fisher Scientific) was performed to determine protein concentrations. Ten micrograms of total protein per sample were mixed with Laemmli buffer (1610737, BioRad) containing 5% dithiothreitol (DTT) and denatured at 95°C for 10 min and then run on Bis-Tris gels (Novex, Invitrogen) in MOPS running buffer. For immunoblots of culture supernatants, cells were treated in OptiMEM (1105802, Gibco). Proteins in the supernatants were precipitated with 4 Vol acetone (V800023, Sigma) overnight at -20°C and pelleted by centrifugation. Pellets were air dried for 10 min, resuspended in 40  $\mu$ l of 2 $\times$  Laemmli loading dye, denatured, and used for immunoblotting.

After SDS-polyacrylamide gel electrophoresis (SDS-PAGE), proteins were transferred onto nitrocellulose membranes using the iBlot transfer system (Invitrogen). Depending on the primary antibody used, the membranes were blocked with either 5% bovine serum albumin (BSA) (A2058, Sigma) or 5% dry-milk (M7409, Sigma) in TBS-T (0.05% Tween-20) for at least 1 hour at room temperature. Incubation with primary antibodies (table S6) was performed at 4°C overnight. Blots were developed by washing with TBS-T, probed with 1:5000 diluted HRP-conjugated secondary antibodies, washed again and imaged on a ChemiDoc MP imaging system (BioRad) using enhanced chemiluminescence (ECL) (Immobilon Western, WBKLS0500, Millipore). For quantification of protein band intensities, images were quantified using FIJI/ImageJ and normalized to the actin loading control of each membrane.

For silver staining of protein gels, after SDS-PAGE, the gels were washed in ddH<sub>2</sub>O and then silver stained following the manufacturer's instructions (Silver Stain Plus Kit, 1610449, BioRad). Similarly, washed gels were used for ProQ Diamond staining following the manufacturer's instructions (Pro-Q Diamond Phosphoprotein Gel Stain, P33300, Invitrogen). Stained gels were imaged on a ChemiDoc MP imaging system (BioRad). Similar to chemiluminescence quantification, protein bands from stained gels were quantified using FIJI ImageJ. Coomassie stain of SDS-PAGE gels was performed using InstantBlue Coomassie Protein Stain (ISB1L, Abcam).

#### GBP1 oligomerization assay

To assess GBP1 oligomerization, a protocol previously published for ASC oligomerization (57) was adapted. In brief, cells were seeded and treated as described above but harvested by scraping in ice-cold PBS containing 2 mM EDTA. Next, cell pellets were washed with PBS plus

2 mM EDTA and resuspended in 200  $\mu$ l of buffer A (20 mM HEPES-KOH pH 7.5, 10 mM KCl, 1.5 mM MgCl<sub>2</sub>, 1 mM EDTA, 1 mM EGTA, 320 mM sucrose) and lysed by passing the suspension through a 25-gauge needle. Lysates were cleared by centrifugation at 1800g and 4°C for 15 min. From this, sample was kept as lysate input control. The remaining supernatant was diluted 2 $\times$  with buffer A, and then 400  $\mu$ l of CHAPS buffer (20 mM HEPES-KOH pH 7.5, 5 mM MgCl<sub>2</sub>, 0.5 mM EGTA, 0.1% CHAPS) was added. Precipitated GBP1 was pelleted by centrifugation at 7500g for 30 min. Finally, pellets were resuspended in 30  $\mu$ l of CHAPS buffer with 4 mM of disuccinimidyl suberate (DSS) (21655, Thermo Fisher Scientific) and left to cross-link for 30 min at room temperature, pelleted again by centrifugation at 7500g for 30 min and then dissolved in 2 $\times$  Laemmli loading dye. Samples were then analyzed by immunoblotting.

#### Immunoprecipitations

For immunoprecipitations  $5 \times 10^6$  cells were seeded in six-well plates and differentiated, pretreated, and infected as described above. The cells were washed in ice-cold PBS and scraped from the plates. Whole-cell lysates were prepared by adding 500  $\mu$ l of lysis buffer (1% Triton X-100, 20 mM Tris-HCl pH 8.0, 130 mM NaCl, 1 mM DTT, 10 mM sodium fluoride) with added protease and phosphatase inhibitor cocktails and incubating on ice for 15 min. Lysates were cleared by centrifugation at 4°C for 10 min at full speed.

For Flag and HA immunoprecipitations, cleared lysates were added to Flag(M2)-agarose beads (A2220, Sigma) or Pierce Anti-HA Agarose beads (26182, Thermo Fisher Scientific) pre-equilibrated by washing three times with lysis buffer. Proteins were captured by incubation on a rotator overnight at 4°C. Beads were washed once with lysis buffer, three times with lysis buffer containing 260 mM NaCl, and again twice with lysis buffer. Proteins were eluted using 200 ng/ml 3xFlag peptide (F4799, Sigma) or 200 ng/ml HA peptide (I2149, Sigma) in lysis buffer by incubation on an orbital shaker (1400 rpm) for 2 hours at room temperature.

For immunoprecipitation of endogenous GBP1/GBP1pS156, 2  $\mu$ g of antibodies against the proteins and 50  $\mu$ l of protein G sepharose beads (ab193259, Abcam) were added per 1 ml of lysates (~2 mg of protein) and incubated on a rotator overnight at 4°C. Beads were washed with lysis buffer five times, and proteins were eluted by acidification with 50  $\mu$ l of 0.2 M glycine pH 2.0 followed by an immediate wash with 50  $\mu$ l of lysis buffer. Input, unbound, and elution fractions were kept during immunoprecipitations and analyzed by immunoblotting.

#### Semiquantitative immunoprecipitation

To determine the affinity of GBP1 binding to 14-3-3 proteins, we adapted a previously published



protocol for semiquantitative coimmunoprecipitation (58). For this, HA-tagged 14-3-3 proteins were produced by transfection of HEK293T cells and purified by HA immunoprecipitation. Proteins were eluted using HA peptide and concentrated using 10-kDa cutoff Amicon Ultra-15 Centrifugal Filters (UFC901024, Merck Millipore), exchanging the buffer with binding buffer (25 mM HEPES pH 7.3, 100 mM NaCl, 0.01% Triton X-100, 5% Glycerol, 1 mM DTT). Phosphorylated GBP1pS156 was purified from IFN- $\gamma$ - and Dox-treated THP-1ΔGBP1+Tet-Flag-GBP1 WT cells using the GBP1pS156 antibody, and the protein was concentrated with 50-kDa cutoff Amicon Ultra-15 Centrifugal Filters (UFC905024, Merck Millipore), exchanging the buffer with binding buffer. Next, the purified and phosphorylated Flag-GBP1 was bound to Flag(M2)-agarose beads (A2220, Sigma) by rotating at 4°C overnight and washed with binding buffer, and the beads were blocked with 50 mM ethanolamine in PBS. Finally, 10  $\mu$ l of prepared and washed GBP1 bait beads were incubated with different concentrations of purified 14-3-3 proteins for 1 hour at 4°C and then washed five times with binding buffer. GBP1 and bound 14-3-3 proteins were eluted by boiling the beads in 2 $\times$  Laemmli loading dye. Finally, obtained samples were analyzed by immunoblotting, and blots were quantified using FIJI/ImageJ.

### MS analysis of GBP1 phosphorylation

In vitro kinase assay samples (with ATP and without ATP) were aliquoted in three technical replicates per condition and diluted with 8 M urea to 25 mM Tris-HCl, 4 M urea, 5 mM MgCl<sub>2</sub>. Proteins were reduced with 5 mM Tris(2-carboxyethyl)phosphine-hydrochloride (TCEP) for 30 min at 37°C and alkylated with 10 mM iodoacetamide (IAA) for 30 min at room temperature in the dark. Subsequently, protein samples were loaded onto a 30-kDa molecular weight cutoff filter (MWCO) (Sartorius, VIVACON 500, VN01H22) and washed three times with 50 mM ammonium bicarbonate (Ambic) by centrifugation at 14,000g. Proteins were digested with GluC (Promega, V1651) in 50 mM Ambic at a protease/protein (w/w) ratio of 1:20 at 37°C overnight. Peptides were eluted by centrifugation at 14,000g, and the 30-kDa MWCO filter was washed once with 50 mM Ambic. Peptides were cleaned with C18 UltraMicroSpin columns (The Nest Group) following the manufacturer's recommendation and dried in a SpeedVac concentrator (Thermo Fisher Scientific).

Peptides were reconstituted in 3% acetonitrile (ACN)/0.1% formic acid (FA)/H<sub>2</sub>O, and 0.5  $\mu$ g per sample was subjected to liquid chromatography-MS/MS (LC-MS/MS) using an nLC1000 coupled to an Orbitrap Fusion Tribrid mass spectrometer (Thermo Fisher Scientific). Peptides were loaded onto a 30-cm

column (75- $\mu$ m ID, New Objective) with mobile phase buffer A containing 0.1% FA/H<sub>2</sub>O and separated by reverse-phase liquid chromatography at a ReproSil-Pur 120 A C18-AQ 1- $\mu$ m stationary phase (Dr. Maisch HPLC GmbH). Peptides were eluted with mobile phase buffer B, which consists of 99.9% ACN/0.1% FA, starting with 5% B and increasing up to 50% B in 100 min. LC-MS/MS measurements were acquired in data-dependent mode. MS1 spectra were recorded from 200 to 2000  $m/z$  with a resolution of 120,000 at 200  $m/z$  in the Orbitrap analyzer. MS1 scans were triggered at an AGC target of  $1 \times 10^6$  and maximum injection time in auto mode. Within a cycle time of 3 s, peptides were iteratively isolated with a 1.3- $m/z$  isolation window and fragmented by ETD with automatic charge-dependent determined ETD parameters. MS2 scans were recorded in the Orbitrap analyzer upon reaching the AGC target of  $5 \times 10^4$  with injection time in auto mode. Fragment ions were monitored with a resolution of 60,000 at 200  $m/z$ . Fragmented peptides were dynamically excluded from further analysis for 30 s. Ions with charge state unassigned, 1, or >6 were excluded from fragmentation.

Data-dependent acquisition (DDA) raw data were processed using MaxQuant (v1.5.6) (59). Spectra were searched against the sequences for recombinant GBP1 and PIM1, as well as the proteome sequences of *Escherichia coli* (strain B / BL21-DE3) (tax ID: 469008) and *Trichoplusia ni* (tax ID: 7111), all retrieved from UniProtKB (accessed on 30.05.2021), and common contaminations. Default parameters of MaxQuant were applied while choosing the protease GluC, allowing four miss cleavages, setting the variable modifications to Oxidation (M), Acetyl (Protein N-term), and Phospho (STY), and fixed modification to Carbamidomethyl (C). A false discovery rate (FDR) of 0.01 was controlled at peptide spectrum match, posttranslational modification (PTM) site, and protein level by MaxQuant. Phosphosite localization was automatically calculated by PTM Score of Andromeda within the MaxQuant proteomic suite. Phosphosite data were further analyzed with Perseus (v1.6.10.50). Phosphosites were filtered for a minimum localization probability of >0.75 and minimum three measurements in total across all conditions. A peaklist of ETD-activated MS/MS spectrum for GBP1pS156, preprocessed by Andromeda/MaxQuant, was exported from the MaxQuant viewer and annotated with Interactive Peptide Spectral Annotator (60), considering c-, z-, and y-type fragment ions. The mass spectrometry proteomics data have been deposited to the ProteomeXchange Consortium via the PRIDE (61) partner repository with the dataset identifier PXD030010.

### Identification of GBP1-interacting proteins by MS

Six-well plates were seeded with 10<sup>7</sup> THP-1ΔGBP1+Tet-Flag-GBP1 cells, and the cells were

differentiated, pretreated with IFN- $\gamma$  and Dox, and infected with Tg. Cells were washed in ice-cold PBS, scraped from the plates, pelleted by centrifugation, and washed in PBS. Whole-cell lysates were prepared by adding 500  $\mu$ l of lysis buffer (1% Triton X-100, 20 mM Tris-HCl pH 8.0, 130 mM NaCl, 1 mM DTT, 10 mM sodium fluoride) with added protease and phosphatase inhibitor cocktails and incubation for 15 min on ice. Lysates were cleared by high-speed centrifugation and used for Flag immunoprecipitation. The samples were run on a 12% Bis-Tris polyacrylamide gel until the running front had entered the gel ~5 mm. Samples were excised from the gel, destained with 50% acetonitrile/50 mM ammonium bicarbonate, reduced with 10 mM DTT, and alkylated with 55 mM IAA. After alkylation, proteins were digested with 250 ng of trypsin overnight at 37°C, and the peptides were extracted in 2% formic acid and 1% acetonitrile and speed vacuum dried.

The peptides were reconstituted in 50  $\mu$ l of 0.1% trifluoroacetic acid (TFA) before analysis and loaded on a 50-cm EASY-Spray column (75- $\mu$ m inner diameter, 2- $\mu$ m particle size, Thermo Fisher Scientific) equipped with an integrated electrospray emitter. Reverse-phase LC was performed using the RSLC nano U3000 (Thermo Fisher Scientific) with a binary buffer system at a flow rate of 275 nl/min. Buffer A was 0.1% FA and 5% DMSO, and buffer B was 80% acetonitrile, 0.1% FA, and 5% DMSO. The samples were run on a linear gradient of buffer B (2 to 30%) in 95.5 min. The nano LC was coupled to an Orbitrap Fusion Lumos mass spectrometer using an EASY-Spray nano source (Thermo Fisher Scientific). The Orbitrap Fusion Lumos was operated in DDA mode acquiring MS1 scan (R = 120,000) in the Orbitrap, followed by higher-energy collisional dissociation (HCD) MS2 scans in the Ion Trap. Top Speed acquisition algorithm with a cycle time of 3 s was used to determine the number of selected precursor ions for fragmentation. The dynamic exclusion was set at 30 s. For ion accumulation, the MS1 target was set to  $4 \times 10^5$  ions and the MS2 target to  $2 \times 10^3$  ions. The maximum ion injection time used for MS1 scans was 50 ms and that for MS2 scans was 300 ms. The HCD normalized collision energy was set at 28, and the ability to inject ions for all available parallelizable time was set to "true."

Orbitrap .RAW files were analyzed by MaxQuant (version 1.6.0.13) using Andromeda for peptide search. For identification, peptide length was set to seven amino acids, and match between runs was enabled. Parent ion and tandem mass spectra were searched against UniprotKB *Homo sapiens* (tax ID: 9606) and Tg (tax ID: 1080348) databases. For the search, the enzyme specificity was set to trypsin, with a maximum of two missed cleavages. The precursor mass tolerance was set to 20 parts per million (ppm)

for the initial search (used for mass recalibration) and to 6 ppm for the main search. Product mass tolerance was set to 20 ppm. Fixed modification was defined as cysteine carbamidomethylation. Methionine oxidation and N-terminal protein acetylation were searched as variable modifications. The datasets were filtered on posterior error probability to achieve 1% FDR on the protein level. Quantification was performed with the LFQ algorithm in MaxQuant using three replicate measurements per experiment. Results were compared against the CRAPome database (62) to eliminate common contaminants of Flag immunoprecipitations (data S3 and S4). The MS proteomics data have been deposited to the ProteomeXchange Consortium via the PRIDE (61) partner repository with the dataset identifier PXD029463.

### *In vitro kinase assay*

To determine *in vitro* kinase activity of PIM1 (PV3503, Thermo Fisher Scientific), PIM2 (PV3649, Thermo Fisher Scientific), PIM3 (A30516, Thermo Fisher Scientific), and Akt1/PKB (P2999, Thermo Fisher Scientific) against GBP1 (ab114960, Abcam), the recombinant proteins were mixed with 100  $\mu$ M ATP (PV3227, Thermo Fisher Scientific) in kinase buffer (50 mM Tris-HCl pH 7.4, 10 mM MgCl<sub>2</sub>) and allowed to incubate for 30 min at 30°C. Reactions were stopped by addition of Laemmli buffer containing 5% DTT and denaturing at 95°C for 5 min before analysis by immunoblotting or silver stain.

### *GTPase assay*

To determine GTPase activity, 2  $\mu$ M GBP1, *in vitro* phosphorylated GBP1, or purified GBP1:14-3-3 $\sigma$  complex was incubated with 1 mM of GTP in reaction buffer (40 mM Tris pH 7.5, 80 mM NaCl, 8 mM MgCl<sub>2</sub>, 1 mM EDTA) at room temperature. The concentration of free phosphate product was subsequently determined using Malachite Green Phosphate Assay Kit (MAK307, Sigma) by measuring absorbance at 620 nm and interpolating a phosphate standard curve.

### *Antibody binding assay*

Enzyme-linked immunosorbent assay (ELISA) plates were coated with 1  $\mu$ M phosphorylated or unphosphorylated GBP1 peptides in 100  $\mu$ l of coating buffer (50 mM carbonate/bicarbonate pH 9.6) at 4°C overnight. Plates were washed with TBS-T and blocked with 1% BSA in TBS-T for 1 hour at room temperature. Plates were washed again, and GBP1pS156 antibody was added in different dilutions in blocking buffer and left to bind at 4°C overnight. Plates were washed and probed with horseradish peroxidase (HRP)-conjugated anti-rabbit secondary antibody and developed with TMB solution (N301, Thermo Fisher Scientific) for 10 min at room temperature. The reaction was quenched by the addition of 2 N H<sub>2</sub>SO<sub>4</sub>, and absorption was

quantified on a plate reader (Fluostar Omega, BMG Labtech).

### *ITC*

ITC was performed on a MicroCal VP-ITC. For each titration, 14-3-3 $\sigma$  and GBP1 or previously *in vitro* phosphorylated GBP1 were dialyzed into reaction buffer (50 mM HEPES pH 7.4, 150 mM KCl). Titrations were performed at 25°C with serial injections of 7- $\mu$ l aliquots of 14-3-3 $\sigma$  (125 or 250  $\mu$ M) into a solution of GBP1 or GBP1pS156 (12.5 or 25  $\mu$ M, respectively) in the calorimeter cell (volume 1.3 ml). Data were analyzed with ORIGIN software (MicroCal).

### *Fixed immunofluorescence microscopy*

For imaging,  $0.25 \times 10^6$  cells were seeded on coverslips in 24-well plates. After differentiation, treatments, and infection, cells were washed three times with warm PBS before fixation and then fixed with 4% methanol-free formaldehyde (28906, Thermo Fisher Scientific) for 15 min at room temperature. Fixed cells were washed with PBS and kept at 4°C overnight. Fixed specimens were permeabilized with PermQuench buffer [0.2% (w/v) BSA and 0.02% (w/v) saponin in PBS] for 30 min at room temperature and then stained with primary antibodies for 1 hour at room temperature. After three washes with PBS, cells were incubated with secondary antibody and 1  $\mu$ g/ml Hoechst 33342 (H3570, Invitrogen) diluted in PermQuench buffer for 1 hour at room temperature. Coverslips were extensively washed with PBS and once with ddH<sub>2</sub>O and mounted using 5  $\mu$ l of Mowiol. Specimens were imaged on a Leica SP5-inverted confocal microscope at 100 $\times$  magnification.

### *High-throughput imaging*

For infection analysis,  $5 \times 10^4$  THP-1s were seeded per well of a black-wall, clear-bottom 96-well imaging plate (Thermo Fisher Scientific), differentiated, treated, and infected as described above. Following fixation with 4% methanol-free formaldehyde, specimens were permeabilized and stained with 1  $\mu$ g/ml Hoechst 33342 and 2  $\mu$ g/ml CellMask Deep Red plasma membrane stain (C10046, Invitrogen) at room temperature for 1 hour. After staining, the specimens were extensively washed with PBS and kept in PBS for imaging.

For recruitment analysis, the cells were prepared as described above but were seeded on black-wall, glass-bottom 96-well imaging plates CG 1.0 (130-098-264, MACS Miltenyi Biotec). After fixation, cells were permeabilized and stained with primary antibody diluted in PermQuench buffer for 1 hour at room temperature. After three washes with PBS, cells were incubated with the appropriated secondary antibody and 1  $\mu$ g/ml Hoechst 33342 diluted in PermQuench buffer for 1 hour at room temperature. Then, the specimens were extensively washed with PBS and kept in PBS for imaging.

Imaging for infection analysis used a Cell Insight CX7 High-Content Screening Platform (Thermo Fisher Scientific) or a Celldiscoverer 7 (Zeiss) using 10 $\times$  magnification. For recruitment analysis, plates were imaged on an Opera Phenix High-Content Screening System (PerkinElmer) or a Celldiscoverer 7 (Zeiss) using 20 $\times$ /40 $\times$  magnification. After image acquisition, the images were fed into the Host Response to Microbe Analysis (HRMAN) analysis pipeline (63, 64).

### *Vacuole and parasite breakage assay*

For quantification of Tg vacuole integrity, cells seeded in black-wall 96-well imaging plates were infected and treated as described above. One hour before fixation, 1  $\mu$ g/ml HCS CellMask Deep Red (H32721, Invitrogen) was added to the culture medium to load the cytosol of host cells with this fluorescent dye. After fixation and staining with Hoechst 33342, plates were imaged at 20 $\times$  magnification on a Celldiscoverer 7 (Zeiss). Fluorescence of the dye within detected Tg vacuoles was then analyzed using HRMAN. For analysis of parasite disruption, cells expressing GFP<sub>11</sub> fragment were infected with type II (Pru) Tg $\Delta$ Hpt+GFP<sub>1-10</sub>-expressing parasites. After the infection time course, cells were fixed, stained with Hoechst and anti-Tg-SAG1, imaged, and analyzed for GFP fluorescence using HRMAN, as described previously (13).

### *Fluorescence recovery after photobleaching*

Quantification of GBP1 recruitment dynamics was performed using fluorescence recovery after photobleaching (FRAP). For this,  $0.1 \times 10^6$  THP-1 cells were seeded per well of an eight-well ibidi  $\mu$ -slide (80826, ibidi) differentiated, treated, and infected with Tg as described above. At 2 hours after infection, the specimens were moved to a Leica SP5-inverted confocal microscope. The experiment was performed using the LAS software FRAP-wizard with the following parameters: 256 by 256 pixels, 1400-Hz line frequency scan speed with bidirectional scan, 2 Airy unit (AU) pinhole size, and bleaching laser power at 100%. After selection of the bleach area on Tg vacuoles, the experiment was performed with the following time course: 10 frames at 120 ms prebleach, 1 frame at 120 ms bleach, 100 frames at 120 ms postbleach I, 10 frames at 1 s postbleach II, and 10 frames at 5 s postbleach III. After acquisition, data was double normalized (65) to correct for acquisition bleaching. Finally, using curve fit, the half-time of recovery was determined as a measurement for the mobility of the molecules.

### *Imaging quantifications*

Most quantifications of images were performed using HRMAN (63, 64). HRMAN was used for quantification of Tg growth, Golgi fragmentation, recruitment of proteins to pathogen vacuoles, and measurement of cell shapes, sizes and fluorescence properties. The Pearson's



correlation coefficient for colocalization analysis was computed using Coloc2 FIJI plugin (66). The average distance of GBP1 aggregates to the nucleus was determined using AggreCount (67). Golgi localization of GBP1 was quantified by determining the mean fluorescence intensity (MFI) of GBP1 in the GM130<sup>+</sup> area and divided by the MFI of the respective cell cytosol to normalize for uneven expression.

#### Recombinant protein expression and purification

GBP1 and 14-3-3 $\sigma$  ORFs were amplified from pLenti-Tet-GBP1 and pLenti-Tet-14-3-3 $\sigma$  and ligated into NdeI- and BamHI-digested pET15d vector, pretagged N-terminally with an MBP-8 $\times$ His-3C or 6 $\times$ His-3C sequence using Gibson assembly to obtain pET15d-MBP-8 $\times$ His-3C-GBP1 and pET15d-6 $\times$ His-3C-14-3-3 $\sigma$ , respectively. Plasmids were transformed into BL21 *E. coli*. Bacteria from a single colony were picked and grown in a 10 ml of LB plus ampicillin (EU0400-D, Euromedex) starter culture overnight. Starter cultures were used to inoculate 12 liters of LB plus ampicillin cultures (1:1000 dilution), which were grown to OD<sub>600</sub> ~ 0.9. Protein expression was induced by the addition of 1  $\mu$ M  $\beta$ -D-1-thiogalactopyranoside (IPTG) (EU0008-B, Euromedex). GBP1 was expressed for 16 hours at 18°C and 14-3-3 $\sigma$  at 30°C for 4 hours while shaking at 150 rpm.

Bacteria were harvested by centrifugation, washed with PBS, resuspended in 100 ml of lysis buffer (GBP1: 50 mM HEPES pH 7.8, 30 mM imidazole, 150 mM KCl; 14-3-3 $\sigma$ : 50 mM NaH<sub>2</sub>PO<sub>4</sub> pH 8.0, 10 mM imidazole; 300 mM NaCl), and lysed by sonication on ice (12 min, 1-s pulses with 1-s interruptions). The lysate was cleared by high-speed centrifugation at 20,000g for 1 hour at 4°C and cleared lysate loaded onto a 5-ml Ni-NTA column (ab270529, Abcam). The column was washed with 20 ml of lysis buffer, and bound proteins were eluted with a 40-ml gradient from 30 to 500 mM imidazole in lysis buffer. Target protein-containing fractions were pooled and dialyzed overnight against size exclusion buffer [size exclusion chromatography (SEC) buffer: 50 mM HEPES pH 7.8, 150 mM KCl] while also digesting with His-3C protease (Protein Expression and Purification Core Facility, EMBL Heidelberg). His-3C protease and cleaved tags were removed using reverse immobilized metal affinity chromatography Ni-IMAC purification (635660, Takara), and proteins were concentrated using 50-kDa cutoff spin column concentrators (Amicon Ultra).

The full-length PIM1 ORF was amplified from pLenti-Tet-PIM1 and ligated into BamHI- and HindIII-digested pLIB vector modified with a N-terminal MBP-TEV-SBP tag using Gibson assembly to obtain pLIB-MBP-TEV-SBP-PIM1. The assembled vector was used for Baculovirus generation in SF21 cells (SF21: 11497013, Gibco; SF-900 II SFM: 11497013, Gibco) as described previously (68, 69). Five milliliters of Baculovirus

was used for transfection of 500 ml of Hi5 (*T. ni* High Five Cells: B85502, Invitrogen; ExpressFive SFM, 10486025, Gibco) culture and incubated at 27°C for 72 hours. Hi5 insect cells were harvested by centrifugation, washed with PBS, resuspended in lysis buffer (50 mM HEPES pH 8.0, 300 mM NaCl), and lysed by sonication at 4°C (12 min, 1-s pulses with 1-s interruptions). The lysate was cleared by high-speed centrifugation at 20,000g for 1 hour at 4°C. Cleared lysate was loaded onto preequilibrated amylose resin (E802IS, New England Biolabs) and left to bind for 4 hours at 4°C. The resin was washed with 10 ml of lysis buffer three times, and bound PIM1 was eluted with 30 ml of lysis buffer containing 25 mM maltose. Obtained MBP-TEV-SBP-PIM1 was dialyzed against 50 mM NaH<sub>2</sub>PO<sub>4</sub> pH 8.0, 300 mM NaCl, and 30 mM imidazole buffer overnight while also digesting with His-TEV protease (Protein Expression and Purification Core Facility, EMBL Heidelberg). His-TEV protease and cleaved tags were removed using serial reverse His- and amylose-affinity purification and PIM1 protein concentrated using 30-kDa cutoff spin column concentrators (Amicon Ultra). Bulk-purified GBP1, PIM1, and 14-3-3 $\sigma$  were further purified by SEC with a HiLoad 16/600 Superdex 200 column (Cytiva) in SEC buffer.

#### GBP1:14-3-3 $\sigma$ complex formation and purification

For in vitro reconstitution of the GBP1:14-3-3 $\sigma$  complex, purified GBP1, 14-3-3 $\sigma$ , and PIM1 were mixed in a 2:4:1 ratio in complex formation buffer (Tris-HCl pH 7.4, 150 mM KCl, 10 mM MgCl<sub>2</sub>) with addition of 1 mM ATP and incubated at 30°C for 1 hour. Reaction samples were cleared by centrifugation at 20,000g for 5 min at 4°C and ran over a Superdex 200 Increase 10/300 GL column (Cytiva Lifesciences) in SEC buffer. To further polish for structure analysis, complex-containing fractions were pooled, concentrated with a 100-kDa cutoff spin column concentrator (Amicon Ultra), and re-purified by SEC. To test the effect of 14-3-3 $\sigma$  binding on GBP1 dimerization, samples were additionally incubated with 1 mM GTP or with 1 mM GDP plus 10 mM AlF<sub>3</sub> (449628, Merck).

#### Single-particle cryo-EM and structure modeling

The GBP1:14-3-3 $\sigma$  complex was prepared as described above. Fractions corresponding to a heterotrimeric complex were vitrified in R1.2/R1.3 UltrAuFoil grids with a 300 mesh (Q350AR13A, Electron Microscopy Sciences) that were glow discharged for 20 s at 25 mA and 0.3 bar using a Pelco EasyGlow device. The sample concentration was adjusted to 0.25 mg/ml, and 2- $\mu$ l drops in SEC buffer were applied to either side of the grid. Excess sample was removed by blotting using a VitriBot MARK IV at 4°C and 100% humidity for 2 s with blotting force 10 and subsequently plunge-frozen in

liquid ethane. The vitrified particles were imaged using a FEI Titan Krios cryo-transmission electron microscope (TEM) at 300 kV at EMBL Heidelberg equipped with a GIF Quantum K2 direct electron detector and a GIF quantum energy filter (Gatan). In total, 14,974 movies were collected in counting mode with seven exposures per hole at a nominal magnification of 215,000 $\times$  with a pixel size of 0.638 Å<sup>2</sup>. Each movie was exposed for 8 s, resulting in a total dose of 65.5 e/Å<sup>2</sup> over 40 frames.

All data-processing steps were performed using cryoSPARC v3.2.0 unless stated otherwise (70). Imported movies were subjected to motion correction using the cryoSPARC multipatch motion correction followed by multipatch contrast transfer function (CTF) estimation. Initially, particles were identified by using automated Gaussian picking for elliptical particles with 50 by 120 Å. Picked particles were extracted, fourfold binned, and subjected to extensive two-dimensional (2D) classification, which identified 4129 particles corresponding to the 14-3-3 $\sigma$ /GBP1 complex. The particles were used to train Topaz (71) and repick on all micrographs, yielding 420,768 particles. 2D classification identified 29,150 particles. Ab initio modeling with three models was used to generate preliminary volumes. Reextraction followed by a heterogeneous refinement using the previously determined initial 3D volumes resulted in a similar particle distribution. Class 3 was used to retrain Topaz for automated particle picking. Identified particles were extracted with fourfold binning. Subsequent 2D classification identified 138,809 particles, which were used to generate five new initial models. The particles were reextracted with full pixel size and subjected to heterogeneous refinement with the previously determined 3D volumes. Class 3 yielded a model with 40,112 particles. The corresponding particles were further classified into three ab initio models. A class with 18,717 particles was identified and subjected to nonuniform refinement, yielding a final cryo-EM map at 5.1 Å.

Densities were generated in CryoSPARC and loaded into ChimeraX (version 0.93) (72), and previously reported crystal structures [Protein Data Bank (PDB) IDs 1F5N for GBP1 and 1YWT for 14-3-3 $\sigma$  dimer] were fitted using the program's own density fitting tools. The final model was deposited in the Electron Microscopy Data Bank (EMDB) with accession number EMD-18149, and the rigid body docked model was deposited in the PDB with accession number 8Q4L.

#### Evolutionary analysis of GBP genes

Position-Specific Iterated-Basic Local Alignment Search Tool (PSI-BLAST) (73) searches using full-length GBP1 as query of the RefSeq Protein sequence database identified >3300 GBP1-like proteins from >500 species. Protein sequences were aligned with MAFFT (74), and incomplete



data were removed with MaxAlign v1.1 (75). The closest homolog of human GBP1 could be identified based on sequence homology in 484 species, and the respective sequences were analyzed for the presence of the corresponding phosphoserine and PIM1 recognition motif.

### In silico analysis, data handling, and statistics

Data were plotted using Prism 8.4.0 (GraphPad, Inc.) and presented as means of multiple experiments with error bars as standard deviation (SD), unless stated otherwise. The significance of results was determined by nonparametric one-way analysis of variance (ANOVA), unpaired Student's *t* test, or two-way ANOVA as indicated in the figure legends. Benjamini, Krieger, and Yekutieli FDR ( $Q = 5\%$ )-based correction for multiple comparisons as implemented in Prism was used when making more than three comparisons. Structures of GBP1 were obtained from the PDB database under PDB IDs 1F5N and 1DG3 (76, 77), and images were rendered with MacPymol v.1.74, which was also used for B-factor analysis. Molecular graphics and analyses were performed with UCSF ChimeraX. GBP1 phosphorylation-site data were obtained from [www.phosphosite.org](http://www.phosphosite.org) (accessed 4 January 2019). 14-3-3 binding site identification used 14-3-3-Pred (78). Kinase predictions were performed using NetPhos Server3.1 (79) and GPS5.0 (80), and recognition sequence phosphorylation-likelihood values were obtained from PhosphoNET: Kinexus (<http://www.phosphonet.ca/>). All open-source KNIME workflows used in this work can be found at <https://github.com/HRMan-Org/HRMan> and on the homepage <https://www.hrman.org>.

### REFERENCES AND NOTES

- J. D. MacMicking, Interferon-inducible effector mechanisms in cell-autonomous immunity. *Nat. Rev. Immunol.* **12**, 367–382 (2012). doi: [10.1038/nri3210](https://doi.org/10.1038/nri3210); pmid: [22531325](https://pubmed.ncbi.nlm.nih.gov/22531325/)
- E. A. Van der Biezen, J. D. G. Jones, Plant disease-resistance proteins and the gene-for-gene concept. *Trends Biochem. Sci.* **23**, 454–456 (1998). doi: [10.1016/S0968-0004\(98\)01311-5](https://doi.org/10.1016/S0968-0004(98)01311-5); pmid: [9868361](https://pubmed.ncbi.nlm.nih.gov/9868361/)
- N. Lopes Fischer, N. Naseer, S. Shin, I. E. Brodsky, Effector-triggered immunity and pathogen sensing in metazoans. *Nat. Microbiol.* **5**, 14–26 (2020). doi: [10.1038/s41564-019-0623-2](https://doi.org/10.1038/s41564-019-0623-2); pmid: [31857733](https://pubmed.ncbi.nlm.nih.gov/31857733/)
- K. Tretina, E. S. Park, A. Maminska, J. D. MacMicking, Interferon-induced guanylate-binding proteins: Guardians of host defense in health and disease. *J. Exp. Med.* **216**, 482–500 (2019). doi: [10.1084/jem.20182031](https://doi.org/10.1084/jem.20182031); pmid: [30755454](https://pubmed.ncbi.nlm.nih.gov/30755454/)
- B.-H. Kim et al., A family of IFN- $\gamma$ -inducible 65-kD GTPases protects against bacterial infection. *Science* **332**, 717–721 (2011). doi: [10.1126/science.1201711](https://doi.org/10.1126/science.1201711); pmid: [21551061](https://pubmed.ncbi.nlm.nih.gov/21551061/)
- A. R. Shenoy et al., GBP5 promotes NLRP3 inflammasome assembly and immunity in mammals. *Science* **336**, 481–485 (2012). doi: [10.1126/science.1217141](https://doi.org/10.1126/science.1217141); pmid: [22461501](https://pubmed.ncbi.nlm.nih.gov/22461501/)
- M. P. Wandel et al., Guanylate-binding proteins convert cytosolic bacteria into caspase-4 signaling platforms. *Nat. Immunol.* **21**, 880–891 (2020). doi: [10.1038/s41590-020-0697-2](https://doi.org/10.1038/s41590-020-0697-2); pmid: [32541830](https://pubmed.ncbi.nlm.nih.gov/32541830/)
- M. A. Al-Zeer, H. M. Al-Younes, D. Lauster, M. Abu Lubad, T. F. Meyer, Autophagy restricts *Chlamydia trachomatis* growth in human macrophages via IFN- $\gamma$ -inducible guanylate binding proteins. *Autophagy* **9**, 50–62 (2013). doi: [10.4161/auto.22482](https://doi.org/10.4161/auto.22482); pmid: [23086406](https://pubmed.ncbi.nlm.nih.gov/23086406/)
- A. S. Piro et al., Detection of cytosolic *Shigella flexneri* via a C-terminal triple-arginine motif of GBP1 inhibits actin-based motility. *mBio* **8**, e01979-17 (2017). doi: [10.1128/mBio.01979-17](https://doi.org/10.1128/mBio.01979-17); pmid: [29233899](https://pubmed.ncbi.nlm.nih.gov/29233899/)

- A. Qin et al., Guanylate-binding protein 1 (GBP1) contributes to the immunity of human mesenchymal stromal cells against *Toxoplasma gondii*. *Proc. Natl. Acad. Sci. U.S.A.* **114**, 1365–1370 (2017). doi: [10.1073/pnas.1619665114](https://doi.org/10.1073/pnas.1619665114); pmid: [28123064](https://pubmed.ncbi.nlm.nih.gov/28123064/)
- D. Fisch et al., Human GBP1 is a microbe-specific gatekeeper of macrophage apoptosis and pyroptosis. *EMBO J.* **38**, e100926 (2019). doi: [10.15252/emboj.2018100926](https://doi.org/10.15252/emboj.2018100926); pmid: [31268602](https://pubmed.ncbi.nlm.nih.gov/31268602/)
- A. R. Bass, S. Shin, Human GBP1 promotes pathogen vacuole rupture and inflammasome activation during *Legionella pneumophila* infection. *bioRxiv* 2020.05.27.120477 [Preprint] (2020); <https://doi.org/10.1101/2020.05.27.120477>
- D. Fisch et al., Human GBP1 differentially targets *Salmonella* and *Toxoplasma* to license recognition of microbial ligands and caspase-mediated death. *Cell Rep.* **32**, 108008 (2020). doi: [10.1016/j.celrep.2020.108008](https://doi.org/10.1016/j.celrep.2020.108008); pmid: [32783936](https://pubmed.ncbi.nlm.nih.gov/32783936/)
- M. Kutsch et al., Direct binding of polymeric GBP1 to LPS disrupts bacterial cell envelope functions. *EMBO J.* **39**, e104926 (2020). doi: [10.15252/emboj.2020104926](https://doi.org/10.15252/emboj.2020104926); pmid: [32510692](https://pubmed.ncbi.nlm.nih.gov/32510692/)
- J. C. Santos et al., Human GBP1 binds LPS to initiate assembly of a caspase-4 activating platform on cytosolic bacteria. *Nat. Commun.* **11**, 3276 (2020). doi: [10.1038/s41467-020-16889-z](https://doi.org/10.1038/s41467-020-16889-z); pmid: [32581219](https://pubmed.ncbi.nlm.nih.gov/32581219/)
- N. Britzen-Laurent et al., Intracellular trafficking of guanylate-binding proteins is regulated by heterodimerization in a hierarchical manner. *PLOS ONE* **5**, e14246 (2010). doi: [10.1371/journal.pone.0014246](https://doi.org/10.1371/journal.pone.0014246); pmid: [21151871](https://pubmed.ncbi.nlm.nih.gov/21151871/)
- E. Kravets et al., Guanylate binding proteins directly attack *Toxoplasma gondii* via supramolecular complexes. *eLife* **5**, e11479 (2016). doi: [10.7554/eLife.11479](https://doi.org/10.7554/eLife.11479); pmid: [26814575](https://pubmed.ncbi.nlm.nih.gov/26814575/)
- S. Zhu et al., Cryo-ET of a human GBP coatomer governing cell-autonomous innate immunity to infection. *bioRxiv* 2021.08.26.457804 [Preprint] (2021); <https://doi.org/10.1101/2021.08.26.457804>
- M. Schwemmler, P. Staeheli, The interferon-induced 67-kDa guanylate-binding protein (hGBP1) is a GTPase that converts GTP to GMP. *J. Biol. Chem.* **269**, 11299–11305 (1994). doi: [10.1016/S0021-9258\(19\)78125-3](https://doi.org/10.1016/S0021-9258(19)78125-3); pmid: [7512561](https://pubmed.ncbi.nlm.nih.gov/7512561/)
- N. Modiano, Y. E. Lu, P. Cresswell, Golgi targeting of human guanylate-binding protein-1 requires nucleotide binding, isoprenylation, and an IFN- $\gamma$ -inducible cofactor. *Proc. Natl. Acad. Sci. U.S.A.* **102**, 8680–8685 (2005). doi: [10.1073/pnas.0503227102](https://doi.org/10.1073/pnas.0503227102); pmid: [15937107](https://pubmed.ncbi.nlm.nih.gov/15937107/)
- M. Andreoli et al., Identification of the first inhibitor of the GBP1:PIM1 interaction. Implications for the development of a new class of anticancer agents against paclitaxel resistant cancer cells. *J. Med. Chem.* **57**, 7916–7932 (2014). doi: [10.1021/jm5009902](https://doi.org/10.1021/jm5009902); pmid: [25121704](https://pubmed.ncbi.nlm.nih.gov/25121704/)
- A. Kumar et al., Crystal structures of proto-oncogene kinase Pim1: A target of aberrant somatic hypermutations in diffuse large cell lymphoma. *J. Mol. Biol.* **348**, 183–193 (2005). doi: [10.1016/j.jmb.2005.02.039](https://doi.org/10.1016/j.jmb.2005.02.039); pmid: [15808862](https://pubmed.ncbi.nlm.nih.gov/15808862/)
- M. T. Yip-Schneider, M. Horie, H. E. Broxmeyer, Transcriptional induction of pim-1 protein kinase gene expression by interferon gamma and posttranscriptional effects on costimulation with steel factor. *Blood* **85**, 3494–3502 (1995). doi: [10.1182/blood.V85.12.3494.bloodjournal85123494](https://doi.org/10.1182/blood.V85.12.3494.bloodjournal85123494); pmid: [7540064](https://pubmed.ncbi.nlm.nih.gov/7540064/)
- T. L. T. Aho et al., Pim-1 kinase promotes inactivation of the pro-apoptotic Bad protein by phosphorylating it on the Ser<sup>112</sup> gatekeeper site. *FEBS Lett.* **571**, 43–49 (2004). doi: [10.1016/j.febslet.2004.06.050](https://doi.org/10.1016/j.febslet.2004.06.050); pmid: [15280015](https://pubmed.ncbi.nlm.nih.gov/15280015/)
- A. N. Bullock, J. Debreceeni, A. L. Amos, S. Knapp, B. E. Turk, Structure and substrate specificity of the Pim-1 kinase. *J. Biol. Chem.* **280**, 41675–41682 (2005). doi: [10.1074/jbc.M510711200](https://doi.org/10.1074/jbc.M510711200); pmid: [16227208](https://pubmed.ncbi.nlm.nih.gov/16227208/)
- A. Macdonald et al., Pim kinases phosphorylate multiple sites on Bad and promote 14-3-3 binding and dissociation from Bcl-XL. *BMC Cell Biol.* **7**, 1 (2006). doi: [10.1186/1471-2121-7-1](https://doi.org/10.1186/1471-2121-7-1); pmid: [16403219](https://pubmed.ncbi.nlm.nih.gov/16403219/)
- C. K. Palaty, I. Clark-Lewis, D. Leung, S. L. Pelech, Phosphorylation site substrate specificity determinants for the Pim-1 protooncogene-encoded protein kinase. *Biochem. Cell Biol.* **75**, 153–162 (1997). doi: [10.1139/o97-026](https://doi.org/10.1139/o97-026); pmid: [9250363](https://pubmed.ncbi.nlm.nih.gov/9250363/)
- N. Ostler et al., Gamma interferon-induced guanylate binding protein 1 is a novel actin cytoskeleton remodeling factor. *Mol. Cell Biol.* **34**, 196–209 (2014). doi: [10.1128/MCB.00664-13](https://doi.org/10.1128/MCB.00664-13); pmid: [24190970](https://pubmed.ncbi.nlm.nih.gov/24190970/)
- P. Riou et al., 14-3-3 proteins interact with a hybrid prenyl-phosphorylation motif to inhibit G proteins. *Cell* **153**, 640–653 (2013). doi: [10.1016/j.cell.2013.03.044](https://doi.org/10.1016/j.cell.2013.03.044); pmid: [23622247](https://pubmed.ncbi.nlm.nih.gov/23622247/)
- G. Gay et al., *Toxoplasma gondii* TgIST co-opts host chromatin repressors dampening STAT1-dependent gene regulation and

- IFN- $\gamma$ -mediated host defenses. *J. Exp. Med.* **213**, 1779–1798 (2016). doi: [10.1084/jem.20160340](https://doi.org/10.1084/jem.20160340); pmid: [27503074](https://pubmed.ncbi.nlm.nih.gov/27503074/)
- P. Olias, R. D. Etheridge, Y. Zhang, M. J. Holtzman, L. D. Sibley, *Toxoplasma* effector recruits the Mi-2/NuRD complex to repress STAT1 transcription and block IFN- $\gamma$ -dependent gene expression. *Cell Host Microbe* **20**, 72–82 (2016). doi: [10.1016/j.chom.2016.06.006](https://doi.org/10.1016/j.chom.2016.06.006); pmid: [27414498](https://pubmed.ncbi.nlm.nih.gov/27414498/)
- G. Carbotti et al., Cytokine-induced guanylate binding protein 1 (GBP1) release from human ovarian cancer cells. *Cancers* **12**, 488 (2020). doi: [10.3390/cancers12020488](https://doi.org/10.3390/cancers12020488); pmid: [32093058](https://pubmed.ncbi.nlm.nih.gov/32093058/)
- J. Ma, H. K. Arnold, M. B. Lilly, R. C. Sears, A. S. Kraft, Negative regulation of Pim-1 protein kinase levels by the B56 $\beta$  subunit of PP2A. *Oncogene* **26**, 5145–5153 (2007). doi: [10.1038/sj.onc.1210323](https://doi.org/10.1038/sj.onc.1210323); pmid: [17297438](https://pubmed.ncbi.nlm.nih.gov/17297438/)
- L.-M. Ting, A. C. Kim, A. Cattamanchi, J. D. Ernst, *Mycobacterium tuberculosis* inhibits IFN- $\gamma$  transcriptional responses without inhibiting activation of STAT1. *J. Immunol.* **163**, 3898–3906 (1999). doi: [10.4049/jimmunol.163.7.3898](https://doi.org/10.4049/jimmunol.163.7.3898); pmid: [10490990](https://pubmed.ncbi.nlm.nih.gov/10490990/)
- P. Najjarro, P. Traktman, J. A. Lewis, Vaccinia virus blocks gamma interferon signal transduction: Viral Vh1 phosphatase reverses Stat1 activation. *J. Virol.* **75**, 3185–3196 (2001). doi: [10.1128/JVI.75.7.3185-3196.2001](https://doi.org/10.1128/JVI.75.7.3185-3196.2001); pmid: [11238845](https://pubmed.ncbi.nlm.nih.gov/11238845/)
- D. M. Miller et al., Human cytomegalovirus inhibits major histocompatibility complex class II expression by disruption of the Jak/Stat pathway. *J. Exp. Med.* **187**, 675–683 (1998). doi: [10.1084/jem.187.5.675](https://doi.org/10.1084/jem.187.5.675); pmid: [9480977](https://pubmed.ncbi.nlm.nih.gov/9480977/)
- D. Nandan, N. E. Reiner, Attenuation of gamma interferon-induced tyrosine phosphorylation in mononuclear phagocytes infected with *Leishmania donovani*: Selective inhibition of signaling through Janus kinases and Stat1. *Infect. Immun.* **63**, 4495–4500 (1995). doi: [10.1128/iai.63.11.4495-4500.1995](https://doi.org/10.1128/iai.63.11.4495-4500.1995); pmid: [7591091](https://pubmed.ncbi.nlm.nih.gov/7591091/)
- K. Kumthip et al., Hepatitis C virus NS5A disrupts STAT1 phosphorylation and suppresses type I interferon signaling. *J. Virol.* **86**, 8581–8591 (2012). doi: [10.1128/JVI.00533-12](https://doi.org/10.1128/JVI.00533-12); pmid: [22674974](https://pubmed.ncbi.nlm.nih.gov/22674974/)
- J. J. He et al., Global transcriptome profiling of multiple porcine organs reveals toxoplasma gondii-induced transcriptional landscapes. *Front. Immunol.* **10**, 1531 (2019). doi: [10.3389/fimmu.2019.01531](https://doi.org/10.3389/fimmu.2019.01531); pmid: [31333663](https://pubmed.ncbi.nlm.nih.gov/31333663/)
- S.-Z. Wu et al., Genome-wide CRISPR screen identifies host factors required by *Toxoplasma gondii* infection. *Front. Cell. Infect. Microbiol.* **9**, 460 (2020). doi: [10.3389/fcimb.2019.00460](https://doi.org/10.3389/fcimb.2019.00460); pmid: [32039045](https://pubmed.ncbi.nlm.nih.gov/32039045/)
- L. Zhang, J. Chen, H. Fu, Suppression of apoptosis signal-regulating kinase 1-induced cell death by 14-3-3 proteins. *Proc. Natl. Acad. Sci. U.S.A.* **96**, 8511–8515 (1999). doi: [10.1073/pnas.96.15.8511](https://doi.org/10.1073/pnas.96.15.8511); pmid: [10411906](https://pubmed.ncbi.nlm.nih.gov/10411906/)
- R. Zhang et al., Hsp90-Akt phosphorylates ASK1 and inhibits ASK1-mediated apoptosis. *Oncogene* **24**, 3954–3963 (2005). doi: [10.1038/sj.onc.1208548](https://doi.org/10.1038/sj.onc.1208548); pmid: [15782121](https://pubmed.ncbi.nlm.nih.gov/15782121/)
- J. J. Gu, Z. Wang, R. Reeves, N. S. Magnuson, PIM1 phosphorylates and negatively regulates ASK1-mediated apoptosis. *Oncogene* **28**, 4261–4271 (2009). doi: [10.1038/onc.2009.276](https://doi.org/10.1038/onc.2009.276); pmid: [19749799](https://pubmed.ncbi.nlm.nih.gov/19749799/)
- D. Morishita, R. Katayama, K. Sekimizu, T. Tsuruo, N. Fujita, Pim kinases promote cell cycle progression by phosphorylating and down-regulating p27Kip1 at the transcriptional and posttranscriptional levels. *Cancer Res.* **68**, 5076–5085 (2008). doi: [10.1158/0008-5472.CAN-08-0634](https://doi.org/10.1158/0008-5472.CAN-08-0634); pmid: [18593906](https://pubmed.ncbi.nlm.nih.gov/18593906/)
- R. A. L. van der Hoorn, S. Kamoun, From guard to decoy: A new model for perception of plant pathogen effectors. *Plant Cell* **20**, 2009–2017 (2008). doi: [10.1105/tpc.108.060194](https://doi.org/10.1105/tpc.108.060194); pmid: [18723576](https://pubmed.ncbi.nlm.nih.gov/18723576/)
- I. Jéru et al., Interaction of pyrin with 14.3.3 in an isoform-specific and phosphorylation-dependent manner regulates its translocation to the nucleus. *Arthritis Rheum.* **52**, 1848–1857 (2005). doi: [10.1002/art.21050](https://doi.org/10.1002/art.21050); pmid: [15934090](https://pubmed.ncbi.nlm.nih.gov/15934090/)
- W. Gao, J. Yang, W. Liu, Y. Wang, F. Shao, Site-specific phosphorylation and microtubule dynamics control Pyrin inflammasome activation. *Proc. Natl. Acad. Sci. U.S.A.* **113**, E4857–E4866 (2016). doi: [10.1073/pnas.1601700113](https://doi.org/10.1073/pnas.1601700113); pmid: [27482109](https://pubmed.ncbi.nlm.nih.gov/27482109/)
- S. L. Masters et al., Familial autoinflammation with neutrophilic dermatosis reveals a regulatory mechanism of pyrin activation. *Sci. Transl. Med.* **8**, 332ra45 (2016). doi: [10.1126/scitranslmed.aaf1471](https://doi.org/10.1126/scitranslmed.aaf1471); pmid: [27030597](https://pubmed.ncbi.nlm.nih.gov/27030597/)
- Y. H. Park, G. Wood, D. L. Kastner, J. J. Chae, Pyrin inflammasome activation and RhoA signaling in the autoinflammatory diseases FMF and HIDS. *Nat. Immunol.* **17**, 914–921 (2016). doi: [10.1038/ni.3457](https://doi.org/10.1038/ni.3457); pmid: [27270401](https://pubmed.ncbi.nlm.nih.gov/27270401/)
- M. M. Gaidt et al., Self-guarding of MORC3 enables virulence factor-triggered immunity. *Nature* **600**, 138–142 (2021). doi: [10.1038/s41586-021-04054-5](https://doi.org/10.1038/s41586-021-04054-5); pmid: [34759314](https://pubmed.ncbi.nlm.nih.gov/34759314/)

51. M. H. Orzalli *et al.*, Virus-mediated inactivation of anti-apoptotic Bcl-2 family members promotes Gasdermin-E-dependent pyroptosis in barrier epithelial cells. *Immunity* **54**, 1447–1462.e5 (2021). doi: [10.1016/j.immuni.2021.04.012](https://doi.org/10.1016/j.immuni.2021.04.012); pmid: [33979579](https://pubmed.ncbi.nlm.nih.gov/33979579/)
52. K. Wanigasooriya *et al.*, Patient derived organoids confirm that PI3K/AKT signalling is an escape pathway for radioresistance and a target for therapy in rectal cancer. *Front. Oncol.* **12**, 920444 (2022). doi: [10.3389/fonc.2022.920444](https://doi.org/10.3389/fonc.2022.920444); pmid: [35860583](https://pubmed.ncbi.nlm.nih.gov/35860583/)
53. N. E. Sanjana, O. Shalem, F. Zhang, Improved vectors and genome-wide libraries for CRISPR screening. *Nat. Methods* **11**, 783–784 (2014). doi: [10.1038/nmeth.3047](https://doi.org/10.1038/nmeth.3047); pmid: [25075903](https://pubmed.ncbi.nlm.nih.gov/25075903/)
54. Z. Dwyer, R. Palais, C. T. Wittwer, uMELT: Prediction of high-resolution melting curves and dynamic melting profiles of PCR products in a rich web application. *Bioinformatics* **27**, 1019–1020 (2011). doi: [10.1093/bioinformatics/btr065](https://doi.org/10.1093/bioinformatics/btr065); pmid: [21300699](https://pubmed.ncbi.nlm.nih.gov/21300699/)
55. E. W. Wilker, R. A. Grant, S. C. Artim, M. B. Yaffe, A structural basis for 14-3-3 functional specificity. *J. Biol. Chem.* **280**, 18891–18898 (2005). doi: [10.1074/jbc.M500982200](https://doi.org/10.1074/jbc.M500982200); pmid: [15731107](https://pubmed.ncbi.nlm.nih.gov/15731107/)
56. F. Q. Li, A. Mofunanya, K. Harris, K. Takemaru, Chibby cooperates with 14-3-3 to regulate  $\beta$ -tubulin subcellular distribution and signaling activity. *J. Cell Biol.* **181**, 1141–1154 (2008). doi: [10.1083/jcb.200709091](https://doi.org/10.1083/jcb.200709091); pmid: [18573912](https://pubmed.ncbi.nlm.nih.gov/18573912/)
57. J. Lugin, F. Martinon, Detection of ASC oligomerization by Western blotting. *Bio Protoc.* **7**, ... (2017). doi: [10.21769/BioProtoc.2292](https://doi.org/10.21769/BioProtoc.2292); pmid: [29085861](https://pubmed.ncbi.nlm.nih.gov/29085861/)
58. S. Lapetina, H. Gil-Henn, A guide to simple, direct, and quantitative in vitro binding assays. *J. Biol. Methods* **4**, e62 (2017). doi: [10.14440/jbm.2017.161](https://doi.org/10.14440/jbm.2017.161); pmid: [31453222](https://pubmed.ncbi.nlm.nih.gov/31453222/)
59. J. Cox, M. Mann, MaxQuant enables high peptide identification rates, individualized p.p.b.-range mass accuracies and proteome-wide protein quantification. *Nat. Biotechnol.* **26**, 1367–1372 (2008). doi: [10.1038/nbt.1511](https://doi.org/10.1038/nbt.1511); pmid: [19029910](https://pubmed.ncbi.nlm.nih.gov/19029910/)
60. D. R. Brademan, N. M. Riley, N. W. Kwiecien, J. J. Coon, Interactive Peptide Spectral Annotator: A versatile web-based tool for proteomic applications. *Mol. Cell. Proteomics* **18**, S193–S201 (2019). doi: [10.1074/mcp.TIR118.001209](https://doi.org/10.1074/mcp.TIR118.001209); pmid: [31088857](https://pubmed.ncbi.nlm.nih.gov/31088857/)
61. Y. Perez-Riverol *et al.*, The PRIDE database and related tools and resources in 2019: Improving support for quantification data. *Nucleic Acids Res.* **47**, D442–D450 (2019). doi: [10.1093/nar/gky1106](https://doi.org/10.1093/nar/gky1106); pmid: [30395289](https://pubmed.ncbi.nlm.nih.gov/30395289/)
62. D. Mellacheruvu *et al.*, The CRAPome: A contaminant repository for affinity purification-mass spectrometry data. *Nat. Methods* **10**, 730–736 (2013). doi: [10.1038/nmeth.2557](https://doi.org/10.1038/nmeth.2557); pmid: [23921808](https://pubmed.ncbi.nlm.nih.gov/23921808/)
63. D. Fisch *et al.*, Defining host-pathogen interactions employing an artificial intelligence workflow. *eLife* **8**, e40560 (2019). doi: [10.7554/eLife.40560](https://doi.org/10.7554/eLife.40560); pmid: [30744806](https://pubmed.ncbi.nlm.nih.gov/30744806/)
64. D. Fisch *et al.*, HRMan 2.0: Next-generation artificial intelligence-driven analysis for broad host-pathogen interactions. *Cell. Microbiol.* **23**, e13349 (2021). doi: [10.1111/cmi.13349](https://doi.org/10.1111/cmi.13349); pmid: [33930228](https://pubmed.ncbi.nlm.nih.gov/33930228/)
65. M. Kang, M. Andreani, A. K. Kenworthy, Validation of normalizations, scaling, and photofading corrections for FRAP data analysis. *PLOS ONE* **10**, e0127966 (2015). doi: [10.1371/journal.pone.0127966](https://doi.org/10.1371/journal.pone.0127966); pmid: [26017223](https://pubmed.ncbi.nlm.nih.gov/26017223/)
66. J. Schindelin *et al.*, Fiji: An open-source platform for biological-image analysis. *Nat. Methods* **9**, 676–682 (2012). doi: [10.1038/nmeth.2019](https://doi.org/10.1038/nmeth.2019); pmid: [22743772](https://pubmed.ncbi.nlm.nih.gov/22743772/)
67. J. A. Klickstein, S. Mukkavalli, M. Raman, AggreCount: An unbiased image analysis tool for identifying and quantifying cellular aggregates in a spatially defined manner. *J. Biol. Chem.* **295**, 17672–17683 (2020). doi: [10.1074/jbc.RA120.015398](https://doi.org/10.1074/jbc.RA120.015398); pmid: [33454006](https://pubmed.ncbi.nlm.nih.gov/33454006/)
68. I. Berger, D. J. Fitzgerald, T. J. Richmond, Baculovirus expression system for heterologous multiprotein complexes. *Nat. Biotechnol.* **22**, 1583–1587 (2004). doi: [10.1038/nbt1036](https://doi.org/10.1038/nbt1036); pmid: [15568020](https://pubmed.ncbi.nlm.nih.gov/15568020/)
69. C. Bieniossek, T. Imasaki, Y. Takagi, I. Berger, MultiBac: Expanding the research toolbox for multiprotein complexes. *Trends Biochem. Sci.* **37**, 49–57 (2012). doi: [10.1016/j.tibs.2011.10.005](https://doi.org/10.1016/j.tibs.2011.10.005); pmid: [22154230](https://pubmed.ncbi.nlm.nih.gov/22154230/)
70. A. Punjani, J. L. Rubinstein, D. J. Fleet, M. A. Brubaker, cryoSPARC: Algorithms for rapid unsupervised cryo-EM structure determination. *Nat. Methods* **14**, 290–296 (2017). doi: [10.1038/nmeth.4169](https://doi.org/10.1038/nmeth.4169); pmid: [28165473](https://pubmed.ncbi.nlm.nih.gov/28165473/)
71. T. Bepler *et al.*, Positive-unlabeled convolutional neural networks for particle picking in cryo-electron micrographs. *Nat. Methods* **16**, 1153–1160 (2019). doi: [10.1038/s41592-019-0575-8](https://doi.org/10.1038/s41592-019-0575-8); pmid: [31591578](https://pubmed.ncbi.nlm.nih.gov/31591578/)
72. E. F. Pettersen *et al.*, UCSF ChimeraX: Structure visualization for researchers, educators, and developers. *Protein Sci.* **30**, 70–82 (2021). doi: [10.1002/pro.3943](https://doi.org/10.1002/pro.3943); pmid: [32881101](https://pubmed.ncbi.nlm.nih.gov/32881101/)
73. S. F. Altschul *et al.*, Gapped BLAST and PSI-BLAST: A new generation of protein database search programs. *Nucleic Acids Res.* **25**, 3389–3402 (1997). doi: [10.1093/nar/25.17.3389](https://doi.org/10.1093/nar/25.17.3389); pmid: [9254694](https://pubmed.ncbi.nlm.nih.gov/9254694/)
74. K. Katoh, D. M. Standley, MAFFT multiple sequence alignment software version 7: Improvements in performance and usability. *Mol. Biol. Evol.* **30**, 772–780 (2013). doi: [10.1093/molbev/mst010](https://doi.org/10.1093/molbev/mst010); pmid: [23329690](https://pubmed.ncbi.nlm.nih.gov/23329690/)
75. R. Gouveia-Oliveira, P. W. Sackett, A. G. Pedersen, MaxAlign: Maximizing usable data in an alignment. *BMC Bioinformatics* **8**, 312 (2007). pmid: [17725821](https://pubmed.ncbi.nlm.nih.gov/17725821/)
76. B. Prakash, L. Renault, G. J. Praefcke, C. Herrmann, A. Wittinghofer, Triphosphate structure of guanylate-binding protein 1 and implications for nucleotide binding and GTPase mechanism. *EMBO J.* **19**, 4555–4564 (2000). doi: [10.1093/emboj/19.17.4555](https://doi.org/10.1093/emboj/19.17.4555); pmid: [10970849](https://pubmed.ncbi.nlm.nih.gov/10970849/)
77. B. Prakash, G. J. K. Praefcke, L. Renault, A. Wittinghofer, C. Herrmann, Structure of human guanylate-binding protein 1 representing a unique class of GTP-binding proteins. *Nature* **403**, 567–571 (2000). doi: [10.1038/35000617](https://doi.org/10.1038/35000617); pmid: [10676968](https://pubmed.ncbi.nlm.nih.gov/10676968/)
78. F. Madeira *et al.*, 14-3-3-Pred: Improved methods to predict 14-3-3-binding phosphopeptides. *Bioinformatics* **31**, 2276–2283 (2015). doi: [10.1093/bioinformatics/btv133](https://doi.org/10.1093/bioinformatics/btv133); pmid: [25735772](https://pubmed.ncbi.nlm.nih.gov/25735772/)
79. N. Blom, T. Sicheritz-Pontén, R. Gupta, S. Gammeltoft, S. Brunak, Prediction of post-translational glycosylation and phosphorylation of proteins from the amino acid sequence. *Proteomics* **4**, 1633–1649 (2004). doi: [10.1002/pmic.200300771](https://doi.org/10.1002/pmic.200300771); pmid: [15174133](https://pubmed.ncbi.nlm.nih.gov/15174133/)
80. C. Wang *et al.*, GPS 5.0: An update on the prediction of kinase-specific phosphorylation sites in proteins. *Genomics Proteomics Bioinformatics* **18**, 72–80 (2020). doi: [10.1016/j.gpb.2020.01.001](https://doi.org/10.1016/j.gpb.2020.01.001); pmid: [32200042](https://pubmed.ncbi.nlm.nih.gov/32200042/)

## ACKNOWLEDGMENTS

We thank all members of the Frickel lab (Crick and University of Birmingham) and the Galej lab (EMBL Grenoble) for helpful discussions. We dedicate this work to the memory of Leo Mercer. We further thank H. Ploegh, J. Langhorne, J. Kagan, C. Reis e Sousa, C. B. Bunce for critical comments on the manuscript. We thank M. Goldberg for providing essential reagents. We thank G. Clark, V. Dearing (Crick Genomics and Equipment Park), M. Howell, O.-R. Song (Crick High Throughput Screening), and the Crick and EMBL Grenoble lab support staff for their help. We thank M. Pelosse for assistance with imaging and managing the EMBL Grenoble eukaryotic expression facility (EEF), S. Schneider for the EM facility support at EMBL Grenoble, F. Weis (EMBL cryo-EM service platform in Heidelberg) for performing data collection, and C. Mas and the biophysical platforms of the Grenoble Instruct-ERIC center (UAR 3518 CNRS-CEA-UGA-EMBL) within the Grenoble Partnership for Structural Biology. We also thank the Jinek group (University of Zürich) for providing IT infrastructure for cryo-EM data processing. **Funding:** This research was funded, in whole or in part, by The Wellcome Trust. D.F. was supported by a Boehringer Ingelheim Fonds PhD fellowship, a Human Frontier Science Program (HFSB) long-term postdoctoral fellowship (LT0006/2022-L), and an EMBO nonstipendiary postdoctoral fellowship (ALTF 491-2022). M.Y. acknowledges support from the Agency for Medical Research

and Development (AMED) Strategic International Collaborative Research Program (JP20jm0210067), Research Program on Emerging and Re-emerging Infectious Diseases (JP20fk0108137), and Japanese Initiative for Progress of Research on Infectious Diseases for Global Epidemic (JP20wm0325010); and a Grant-in-Aid for Transformative Research Area (B) (20B304), for Scientific Research on Innovation Areas (19H04809), for Scientific Research (B) (18KK0226 and 18H02642), and for Scientific Research (A) (19H00970) from the Ministry of Education, Culture, Sports, Science and Technology, Fusion Oriented Research for Disruptive Science and Technology. J.M. was supported by the European Research Council (649101-UbiProPox) and by Core funding to MRC Laboratory for Molecular Cell Biology at University College London (MC\_UU\_00012/7). A.R.S. was supported by MRC grant MR/P022138/1. E.-M.F. received funding from Wellcome Trust Senior Research Fellowship 212702/Z/19/Z, MRC Research and Innovation Grant MR/V030930/1 (also to A.R.S.), MRC-AMED grant MR/T029323/1 (also to M.Y.), and core funding to the Francis Crick Institute by Cancer Research UK, the UK Medical Research Council, and the Wellcome Trust (FC001076). K.M.M. acknowledges support from CRUK CEA grant C61638/A27112. A.D.B. is funded by a CRUK Advanced Clinician Scientist Award (C31641/A23923). The Grenoble Instruct-ERIC center (UAR 3518 CNRS-CEA-UGA-EMBL) within the Grenoble Partnership for Structural Biology is supported by FRISBI (ANR-10-INBS-0005-02) and GRAL, which are financed within the University Grenoble Alpes graduate school (Ecoles Universitaires de Recherche) CBH-EUR-GS (ANR-17-EURE-0003). A.P.S. received core funding to the Francis Crick Institute by Cancer Research UK, the UK Medical Research Council, and the Wellcome Trust (FC001999). **Author contributions:** D.F. and E.-M.F. conceived the study. D.F. performed most of the biochemical and functional experiments. D.F., M.M.P., E.A., and X.L. performed protein expression and purification. M.M.P. and X.L. performed single-particle cryo-EM and data analysis and built the structure. F.W. performed MS for mapping of GBPI phosphorylation sites. V.E. performed MS analysis to identify GBPI interactomes. K.M.M., G.M.M., and A.D.B. provided essential reagents and performed organoid culture experiments. H.B. and M.Y. provided essential reagents. E.A., B.C., and S.L.-R. provided essential experimental protocols, assistance, and valuable suggestions. A.P.S., A.R.S., J.M., B.W., W.P.G., and E.-M.F. acquired and contributed funding and experimental oversight. D.F. and E.-M.F. analyzed the data. D.F., E.A., A.R.S., and E.-M.F. wrote the manuscript with input from all authors. All authors discussed the results and commented on the manuscript. **Competing interests:** The authors declare no competing interests. **Data and materials availability:** All data are available in the main text or the supplementary materials. For underlying data, see data S1 to S6. The proteomics raw data have been deposited to PRIDE (PXD029463 and PXD030010). The cryo-EM data have been deposited on EMD (EMD-18149). All specific and stable reagents generated in this study are available from the corresponding author without restriction. **License information:** Copyright © 2023 the authors, some rights reserved; exclusive licensee American Association for the Advancement of Science. No claim to original US government works. <https://www.science.org/about/science-licenses-journal-article-reuse>. This research was funded in whole or in part by The Francis Crick Institute (FC001076 and FC001999), which is funded by Wellcome a cOAlition S organization. The author will make the Author Accepted Manuscript (AAM) version available under a CC BY public copyright license.

## SUPPLEMENTARY MATERIALS

[science.org/doi/10.1126/science.adg2253](https://science.org/doi/10.1126/science.adg2253)

Figs. S1 to S16

Tables S1 to S6

Reference (81)

MDAR Reproducibility Checklist

Data S1 to S6

Submitted 14 December 2022; resubmitted 3 July 2023

Accepted 23 August 2023

10.1126/science.adg2253